Article:
Colombo, M and Fairweather, M (2016) RANS simulation of bubble coalescence and break-up in bubbly two-phase flows. Chemical Engineering Science, 146. pp. 207-225. ISSN 0009-2509

https://doi.org/10.1016/j.ces.2016.02.034

RANS simulation of bubble coalescence and break-up in bubbly two-phase flows

Marco Colombo* and Michael Fairweather

Institute of Particle Science and Engineering, School of Chemical and Process Engineering, University of Leeds, Leeds LS2 9JT, United Kingdom

E-mail addresses: M.Colombo@leeds.ac.uk (Marco Colombo); M.Fairweather@leeds.ac.uk (Michael Fairweather)

*Corresponding Author: +44 (0) 113 343 2351

Abstract

In bubbly flows, the bubble size distribution dictates the interfacial area available for the interphase transfer processes and, therefore, understanding the behaviour and the average features of the bubble population is crucial for the prediction of these kinds of flows. In this work, by means of the STAR-CCM+ code, the S_γ population balance model is coupled with an Eulerian-Eulerian two-fluid approach and tested against data on upward bubbly pipe flows. The S_γ model, based on the moments of the bubble size distribution, tracks the evolution of the bubble sizes due to bubble break-up and bubble coalescence. Good accuracy for the average bubble diameter, the velocity and the void fraction radial profiles is achieved with a modified coalescence source. Numerical results show that better predictions are obtained when these flows are considered to be coalescence dominated, but, nevertheless, additional knowledge is required to progress in the development of coalescence and break-up models that include all the possible responsible mechanisms. In this regard, there is a requirement for experimental data that will allow validation of both the predicted bubble diameter distribution and the intensity of the turbulence in the continuous phase which has a significant impact on coalescence and break-up models. An advanced version of the model described, that

includes a Reynolds stress turbulence formulation and two groups of bubbles to account for the opposite behaviour of spherical bubbles, which accumulate close to the pipe wall, and cap bubbles, that migrate towards the pipe centre, is proposed. The Reynolds stress model is found to better handle the interactions between the turbulence and the interphase forces, and the use of only two bubble groups seems sufficient to describe the whole bubble spectrum and the bubbly flow regime up to the transition to slug flow.

Keywords: Bubbly flow; RANS modelling; population balance; method of moments; bubble diameter distribution.

1. Introduction

Gas-liquid bubbly flows are common to a variety of processes encountered in numerous industrial sectors, including the nuclear sector as well as chemical and petro-chemical, oil and gas, mining, pharmaceutical and refrigeration industries, amongst others. In the nuclear industry, knowledge of the hydrodynamics of the two-phase flow is essential for the design and operation of boiling water reactors and natural circulation systems, and in the prediction of accident scenarios for pressurized water reactors as well as for other types of reactor. In chemical reactors, such as bubble columns and stirred tanks, gas bubbles are dispersed in the liquid phase to increase phase mixing and enhance heat and mass transfer processes.

In these flows, the exchange of mass, momentum and energy between the phases depends on the flow conditions, and on the interfacial area concentration in particular. This, in bubbly flows, is determined by the number and the size of the bubbles that are dispersed in the continuous liquid. Often, bubbles are not monodispersed and their distribution is far from steady, and evolves continuously in space and time, following interactions between the bubbles and the continuous phase and collisions between neighbouring bubbles (Lucas et al., 2005; 2010). These interactions induce bubble shrinkage and growth due to the pressure field and bubble break-up and coalescence, and, in boiling or reacting flows, also wall boiling, evaporation and mass transfer. The bubble distribution is therefore governed by these phenomena that, with bubble behaviour strongly related to bubble size and shape (Tomiyama et al., 1998), determine the local flow field, which, at the same time, affect the ratios of mass transfer, break-up and coalescence. In view of this strong coupling, understanding the evolution of the local bubble size distribution in these kinds of flows still represents a rather complex task which, nevertheless, is necessary if we are to be able to predict them with any degree of accuracy.

The use of computational fluid dynamic (CFD) techniques, applied today in design and as well as a development tool in most of the engineering disciplines, has the potential to significantly improve our ability to predict the mentioned processes. At the present time, application of multiphase CFD to industrial and system-scale calculations has been mainly limited to two-fluid Eulerian-Eulerian, Reynolds-averaged Navier-Stokes (RANS) based models (Prosperetti and Tryggvason, 2009; Tryggvason and Buongiorno, 2010). The use of more advanced techniques, such as direct numerical simulation and large eddy simulation with interface tracking methods (Toutant et al., 2008; Dabiri and Tryggvason, 2015), or Lagrangian tracking techniques (Molin et al., 2012), recently coupled with immersed boundary methods (Santarelli et al., 2015), is mostly constrained to very simple flow conditions in view of the required computational resources (Tryggvason and Buongiorno, 2010).

In two-fluid Eulerian-Eulerian RANS models, the conservation equations for each phase are derived from averaging procedures. Therefore, the details of the interphase structure are not resolved and interface exchange terms require explicit modelling (Fox, 2012; Prosperetti and Tryggvason, 2009). In these models, the bubble diameter is often needed as an input parameter that, therefore, becomes vital to properly predict the fluid dynamic behaviour of the system. Here, possible limitations can be avoided by coupling the CFD model with the population balance equation (PBE) approach which tracks the behaviour of the bubble size distribution in both physical and internal (e.g. bubble diameter or bubble volume) coordinate spaces (Buffo et al., 2013; Marchisio and Fox, 2005). The use of a PBE combined with CFD has been identified as a crucial development for the accurate prediction of bubbly flows, and significant advances have been achieved in recent years using this approach (Buffo et al., 2013; Cheung et al., 2009, 2013; Lehr et al., 2002; Liao et al., 2015; Lo and Zhang, 2009; Marchisio and Fox, 2005, 2007; Nguyen et al., 2013; Yao and Morel, 2004).

Many approaches have been considered for the solution of the PBE within a CFD code (Buffo et al., 2013). In class methods, the internal coordinate space, which is usually the bubble size spectrum, is discretized into numerous size classes and the PBE is integrated over each class to give a finite set of discrete PBEs (Kumar and Ramkrishna, 1996; Liao et al., 2015; Lo, 1996; Nandanwar and Kumar, 2008; Wang et al., 2005). In each class, bubbles may be considered as all having the same size (zero-order methods) or a specified distribution (higher-order methods), often a low-order polynomial (Vanni, 2000). In Monte Carlo methods, stochastic differential equations are solved for a finite number of artificial realizations of the dispersed phase population (Lee and Matsoukas, 2000; Lin et al., 2002; Zhao et al., 2007). For both the class and Monte Carlo methods, the drawback is the high computational cost involved. Respectively, the solution of at least one conservation equation for each class, with all the relevant source and sink terms, is required, or a very high number of realizations is necessary. In the last two decades, many authors have focused their efforts on the development of the interfacial area transport equation, in the context of both two-fluid CFD models and one-dimensional, advanced thermal hydraulic system codes (Hibiki and Ishii, 2000; Nguyen et al., 2013; Smith et al., 2012; Sun et al., 2004; Wu et al., 1998; Yao and Morel, 2004). Being derived from averaging over the whole bubble diameter spectrum, no bubble size distribution is retained and simplifying assumptions are often made, such as the use of constant or simple linear distributions (Ishii and Hibiki, 2006; Smith et al., 2012). Recently, promising results were achieved with progressively more advanced approaches based on the method of moments, originally introduced by Hulburt and Katz (1964). This method is based on the solution of a set of transport equations for the lower-order moments of the dispersed phase distribution (Marchisio and Fox, 2005). Progressively, more advanced methods have been developed, in particular in the category of quadrature-based methods of moments, such as the direct quadrature method (Marchisio and Fox, 2005) and the conditional quadrature method (Yuan and Fox, 2011). Overall, these methods are reported to provide good predictive accuracy without excessive computational cost (Buffo et al., 2013; Marchisio and Fox, 2005). The S_γ model, proposed by Lo

113 and Rao (2007) for droplet two-phase flows, involves a limited number of moments of the bubble
114 size probability distribution, which is assumed to follow a log-normal shape. The model was later
115 extended to bubbly flows by Lo and Zhang (2009) and its ability to predict with a reasonable
116 accuracy a number of different flows was demonstrated.
117
118 Alongside the method of solution, the other key aspect in regards to population balance based
119 approaches is the availability of reliable closure models for the coalescence and break-up
120 mechanisms. This issue has recently been the subject of numerous researches (Liao et al., 2015; Luo
121 and Svendsen, 1996; Mukin, 2014; Prince and Blanch, 1990; Wang et al., 2005; Yao and Morel,
122 2004), and thorough reviews have been provided by Liao and Lucas (2009) for the break-up
123 mechanism and by Liao and Lucas (2010) for the coalescence mechanism. Despite this, however,
124 commonly accepted and reliable models have not yet emerged in view of the intrinsic complexity
125 encountered when modelling coalescence and break-up in turbulent bubbly flows. Amongst others,
126 the strong mutual interactions with the two-phase turbulence, for which a general and mature model
127 is not yet available, and the coupling and relative importance of the different competitive
128 mechanisms (e.g. turbulent collision, wake entrainment, shearing-off) prevent substantial progresses
129 on the subject being achieved and, therefore, further understanding is required. The ongoing
130 modelling effort is supported by the experimental data available from a number of studies
131 (Grossetete, 1995; Hibiki and Ishii, 1999; Hibiki et al., 2001; Liu, 1993; Lucas et al., 2005, 2010;
132 Prasser et al., 2007; Sanyal et al., 1999). In particular, detailed measurements of the average bubble
133 size and the bubble size distribution have been obtained using the wire-mesh sensor technique
134 (Lucas et al., 2005, 2010; Prasser et al., 2007).
135
136 In this paper, the S_γ model, implemented in the STAR-CCM+ code (CD-adapco, 2014), is combined
137 with an Eulerian-Eulerian two fluid model and tested against data on air-water bubbly flows in
138 pipes. With the aim to improve our ability to predict these flows and the evolution of the bubble

diameter distribution, a different coalescence model is introduced and optimized. By means of sensitivity studies, the relative impact of bubble break-up and coalescence, and the influence of the continuous phase turbulence and the bubble-induced turbulence, are investigated. In terms of the turbulent flow field, and in view of the influence it has on the accuracy of the predictions, a Reynolds stress turbulence model is also included with the aim of extending the model's applicability to more complex flows, affected by known shortcomings of two-equation turbulence models. In bubbly flows, which are polydisperse by nature, the size determines the behaviour of the bubble, with small spherical bubbles flowing near the pipe wall and larger, deformed cap bubbles, migrating towards the pipe centre (Tomiyama et al., 2002b). Clearly, predicting this behaviour is mandatory if a general model capable of handling the entire bubble size spectrum is to be developed. In this regard, two bubble classes, each one with its own behaviour, are introduced in the final section of the paper. The ability of such a model, limited to only two bubble classes, to predict the whole bubble spectrum and the transition between wall-peaked and core-peaked void profiles, is then tested.

2. Experimental data

For any CFD technique to be applied with confidence, it is mandatory that the model has been previously validated against relevant experimental data. In this work, seven experiments from Liu (1993), Hibiki and Ishii (1999), Hibiki et al. (2001) and Lucas et al. (2005) were considered. The experimental conditions considered are summarized in Table 1.

Table 1: Experimental database used for validation.

Case	Source	j_w [m s^{-1}]	j_a [m s^{-1}]	α_{avg} [-]	$d_{B,avg}$ [mm]	Re_L [-]
Hi1	Hibiki et al. (2001)	0.986	0.242	0.191	3.4	49989
Hi2	Hibiki et al. (2001)	2.01	0.471	0.230	3.7	101903
HI1	Hibiki and Ishii (1999)	0.262	0.0549	0.245	3.4	6641
HI2	Hibiki and Ishii (1999)	1.75	0.399	0.253	3.8	44361
L1	Liu (1993)	1.0	0.2	0.160	4.2	57086
L2	Liu (1993)	3.0	0.2	0.062	3.4	171257
Lu1	Lucas et al. (2005)	0.255	0.0368	0.072	-	13030

Liu (1993) conducted experiments in a vertical pipe of 0.0572 m i.d. to study the bubble diameter and entrance length effects on the void fraction distribution in upward air-water bubbly flows. Bubble velocity, void fraction and average bubble diameter radial profiles were obtained from measurements at different axial locations. Hibiki and Ishii (1999), and Hibiki et al. (2001), measured water and air velocity, turbulence intensity, void fraction, bubble diameter and interfacial area concentration radial profiles at three consecutive axial locations and for an air-water bubbly flows in vertical pipes of diameter 0.0254 m and 0.0508 m. Lucas et al. (2005) used a wire-mesh sensor to study air-water upward flows inside a 0.0512 m diameter pipe. High-resolution measurements of the void fraction and the bubble diameter distribution were obtained. The experiments extended over a wide range of the bubble diameter spectrum, including some mixed radial void profiles where both spherical and cap bubbles were present, one of which was specifically included in the database to validate the model with two bubble classes. Over the whole database, the water superficial velocity considered is in the range 0.262 m $s^{-1} < j_w < 3.0$ m s^{-1} and the air superficial velocity is in the range 0.0368 m $s^{-1} < j_a < 0.471$ m s^{-1}. Average void fraction α_{avg} and average bubble diameters $d_{B,avg}$ reported in Table 1 were calculated by means of integration of the experimental profiles at the last measurement station. Table 1 also includes values of the Reynolds number of the flows, based on the characteristic dimension along the pipe.

3. Mathematical model

In a two-fluid Eulerian-Eulerian model, each phase is described by a set of averaged conservation equations. As the cases considered in this paper are limited to adiabatic air-water flows, only the continuity and momentum equations are solved, with the phases treated as incompressible with constant properties:

$$\frac{\partial}{\partial t}(\alpha_k \rho_k) + \frac{\partial}{\partial x_i}(\alpha_k \rho_k U_{i,k}) = 0 \quad (1)$$

$$\frac{\partial}{\partial t}\left(\alpha_k \rho_k U_{i,k}\right) + \frac{\partial}{\partial x_j}\left(\alpha_k \rho_k U_{i,k} U_{j,k}\right) = -\alpha_k \frac{\partial}{\partial x_i} p_k + \frac{\partial}{\partial x_j}\left[\alpha_k\left(\tau_{ij,k} + \tau_{ij,k}^{Re}\right)\right] + \alpha_k \rho_k g_i + M_{i,k} \quad (2)$$

189

190 In the above equations, α_k represents the volume fraction of phase k, whereas in the following, only
191 α will be used to specify the void fraction of air. ρ is the density, $\boldsymbol{U}$ the velocity, p the pressure and
192 $\boldsymbol{g}$ the gravitational acceleration. $\boldsymbol{\tau}$ and $\boldsymbol{\tau^{Re}}$ are the laminar and turbulent stress tensors, respectively,
193 and M_k accounts for the momentum exchanges between the phases. In the interfacial term, the drag
194 force, lift force, wall force and turbulent dispersion force are included:

195

$$\boldsymbol{M}_k = \boldsymbol{F}_d + \boldsymbol{F}_l + \boldsymbol{F}_w + \boldsymbol{F}_{td} \quad (3)$$

196

197 The drag force represents the resistance opposed to bubble motion relative to the surrounding liquid
198 and is expressed as:

199

$$\boldsymbol{F}_d = \frac{3}{4}\frac{C_D}{d_B}\alpha\rho_c|\boldsymbol{U}_r|\boldsymbol{U}_r \quad (4)$$

200

201 Here, $\boldsymbol{U_r}$ is the relative velocity between the phases and the subscript c identifies the continuous
202 phase, which is water for all the experiments in Table 1. The drag coefficient, C_D, was calculated
203 using the model of Tomiyama et al. (2002a), where the effect of the bubble aspect ratio on the drag
204 was also accounted for (Hosokawa and Tomiyama, 2009) using:

205

$$C_D = \frac{8}{3}\frac{Eo}{E^{2/3}(1-E^2)^{-1}Eo + 16E^{4/3}}F^{-2} \quad (5)$$

206

207 Here, F is a function of the bubble aspect ratio E. The bubble aspect ratio was derived from the
208 following correlation and as a function of the distance from the wall y_w (Colombo et al., 2015):

209

$$E = \max\left[1.0 - 0.35\frac{y_w}{d_B}, E_0\right] \quad (6)$$

210

211 E_0 is calculated from the expression given by Welleck et al. (1966), where Eo is the Eötvös number:

212

$$E_0 = \frac{1}{1 + 0.163Eo^{0.757}} \quad (7)$$

213

214 A lift force, perpendicular to the direction of motion, is experienced by bubbles moving in a shear
215 flow (Auton, 1987), according to:

216

$$\boldsymbol{F}_l = C_L \alpha \rho_c \boldsymbol{U}_r \text{ x } (\nabla \text{ x } \boldsymbol{U}_c) \quad (8)$$

217

218 In a pipe, the lift force has a strong influence on the radial movement of the bubbles and therefore
219 on the void fraction radial distribution. Generally, a positive value of the lift coefficient C_L
220 characterizes spherical bubbles, which are pushed towards the pipe wall by the lift force. In
221 contrast, larger bubbles, deformed by the inertia of the surrounding liquid, experience a negative lift
222 force and move towards the centre of the pipe (Tomiyama et al., 2002b). In air-water flows, a
223 critical bubble diameter range for the change of sign in the lift coefficient between 5.0 mm and 6.0
224 mm was given by Tomiyama et al. (2002b). These authors also expressed the lift coefficient as a
225 function of the Eötvös number, an approach adopted in other investigations (e.g. Krepper et al.,
226 2008; Rzehak and Krepper, 2013). In this work, however, and in view of previously observed
227 discrepancies between calculations and experimental data when using such an approach, constant
228 values were chosen. More specifically, C_L = 0.1 was used for wall-peaked (Lahey and Drew, 2001;
229 Lopez de Bertodano et al., 1994), and C_L = -0.05 for core-peaked, void profiles.

230

The presence of a solid wall modifies the flow field around the bubbles and the asymmetry in the flow distribution generates a hydrodynamic pressure difference on the bubble surface that keeps bubbles away from the wall (Antal et al., 1991):

$$\boldsymbol{F}_w = \max\left(0, C_{w,1} + C_{w,2}\frac{d_B}{y_w}\right)\alpha\rho_c\frac{|\boldsymbol{U_r}|^2}{d_B}\boldsymbol{n_w} \tag{9}$$

In this equation, $\boldsymbol{n_w}$ is the normal to the wall and C_{w1} and C_{w2} are constants that modulate the strength and the region of influence of the wall force. Here, values of C_{w1} = -0.4 and C_{w2} = 0.3 were used (Colombo et al., 2015). Finally, the turbulent dispersion force was modelled as (Burns et al., 2004):

$$\boldsymbol{F}_{td} = \frac{3}{4}\frac{C_D\alpha\rho_c|\boldsymbol{U}_r|}{d_B}\frac{\nu_{t,c}}{\sigma_\alpha}\left(\frac{1}{\alpha}+\frac{1}{(1-\alpha)}\right)\nabla\alpha \tag{10}$$

where $\nu_{t,c}$ is the turbulent kinematic viscosity of the continuous phase, obtained from the turbulent viscosity $\mu_{t,c}$, calculated from the single-phase relation (more details can be found in the following Section 3.1, where the turbulence model is presented), divided by the continuous phase density ρ_c. σ_α is the turbulent Prandtl number for the void fraction, assumed equal to 1.0 (Burns et al., 2004).

3.1. Multiphase turbulence modelling

Turbulence was solved only in the continuous phase, with a multiphase formulation (CD-adapco, 2014) of the standard *k*-*ε* turbulence model (Jones and Launder, 1972):

$$\begin{aligned}&\frac{\partial}{\partial t}\left((1-\alpha)\rho_c k_c\right)+\frac{\partial}{\partial x_i}\left((1-\alpha)\rho_c U_{i,c} k_c\right)\\&\quad=\frac{\partial}{\partial x_i}\left[(1-\alpha)\left(\mu_c+\frac{\mu_{t,c}}{\sigma_k}\right)\frac{\partial k_c}{\partial x_i}\right]+(1-\alpha)\left(P_{k,c}-\rho_c\varepsilon_c\right)+(1-\alpha)S_k^{BI}\end{aligned} \tag{11}$$

252

$$\frac{\partial}{\partial t}\left((1-\alpha)\rho_c\varepsilon_c\right)+\frac{\partial}{\partial x_i}\left((1-\alpha)\rho_c U_{i,c}\varepsilon_c\right) = \frac{\partial}{\partial x_i}\left[(1-\alpha)\left(\mu_c+\frac{\mu_{t,c}}{\sigma_\varepsilon}\right)\frac{\partial \varepsilon_c}{\partial x_i}\right]+(1-\alpha)\frac{\varepsilon_c}{k_c}\left(C_{\varepsilon,1}P_{k,c}-C_{\varepsilon,2}\rho_c\varepsilon_c\right)+(1-\alpha)S_\varepsilon^{BI} \quad (12)$$

253

254 In the equations above, $P_{k,c}$ is the production term due to shear and S_k^{BI} and S_ε^{BI} the source terms
255 due to bubble-induced turbulence. The turbulent viscosity $\mu_{t,c}$ was evaluated from the single-phase
256 relation:

257

$$\mu_{t,c}=C_\mu\rho_c\frac{k_c^2}{\varepsilon_c} \quad (13)$$

258

259 Turbulence was not resolved in the dispersed phase, but was obtained from the continuous phase.
260 More specifically, it was directly related to the turbulence of the continuous phase by means of a
261 response coefficient C_t, assumed equal to unity (Gosman et al., 1992; Troshko and Hassan, 2001).
262 Experimental measurements do in fact suggest that a value of unity is approached starting from void
263 fractions as small as 6 % (Behzadi et al., 2004).

264

265 In bubby flows, the generation of turbulence by the bubbles often modifies significantly the
266 turbulence in the continuous phase, with respect to the single-phase flow (Lance and Bataille, 1991;
267 Shawkat et al., 2007; Wang et al., 1987). The bubble contribution to turbulence was accounted for
268 with bubble-induced source terms in Eq. (12) and Eq. (13). In particular, the drag force was
269 considered as the only source of turbulence generation due to the bubbles and all the energy lost by
270 the bubbles to drag was assumed to be converted into turbulence kinetic energy inside the bubble
271 wakes (Kataoka and Serizawa, 1989; Rzehak and Krepper, 2013; Troshko and Hassan, 2001):

272

$$S_k^{BI} = K_{BI}\boldsymbol{F_d U_r} \tag{14}$$

273

274 The corresponding turbulence dissipation rate source is equal to the turbulence kinetic energy
275 source divided by the timescale of the bubble-induced turbulence τ_{BI}. In this work, the mixed
276 timescale introduced by Rzehak and Krepper (2013) was chosen, derived from the velocity scale of
277 the turbulence and the length scale of the bubbles:

278

$$S_\varepsilon^{BI} = C_{\varepsilon,BI}\frac{S_k^{BI}}{\tau_{BI}} = 1.0\frac{k^{0.5}}{d_B}S_k^{BI} \tag{15}$$

279

280 The mixed timescale is expected to mimic the split of eddies which move past the bubbles (Rzehak
281 and Krepper, 2013) and the shift of the energy of turbulence to smaller length scales observed in
282 experiments (Lance and Bataille, 1991; Shawkat et al., 2007). The mixed timescale, used in
283 combination with the coefficient K_{BI} = 0.25 in Eq. (14), has been found to provide accurate
284 predictions over a wide range of bubbly pipe flows (Colombo et al., 2015).

285

286 A multiphase Reynolds stress turbulence model (RSM) was also included in the overall model and,
287 based on the single-phase formulation, the Reynolds stresses ($R_{ij} = \tau_{i,j}^{Re}/\rho_c$) are given by (CD-
288 adapco, 2014):

289

$$\begin{aligned}&\frac{\partial}{\partial t}\left((1-\alpha)\rho_c R_{ij}\right) + \frac{\partial}{\partial x_j}\left((1-\alpha)\rho_c U_{i,c} R_{ij}\right)\\ &\qquad = \frac{\partial}{\partial x_j}\left[(1-\alpha)D_{ij}\right] + (1-\alpha)\left(P_{ij} + \Phi_{ij} - \varepsilon_{ij}\right) + (1-\alpha)S_{ij}^{BI}\end{aligned} \tag{16}$$

290

291 Here, P_{ij} is the turbulence production. The Reynolds stress diffusion D_{ij} was modelled accordingly
292 to Daly and Harlow (1970), whilst the isotropic hypothesis was used for the turbulence dissipation

rate term ε_{ij}. Φ_{ij} is the pressure-strain correlation, accounting for pressure fluctuations that redistribute the turbulence kinetic energy amongst the Reynolds stress components. This was modelled using the "SSG model" which is quadratically non-linear in the anisotropy tensor (Speziale et al., 1991):

$$\Phi_{ij} = -[C_{1a}\varepsilon + C_{1b}tr(P)]a_{ij} + C_2\varepsilon\left(a_{ik}a_{kj} - \frac{1}{3}a_{mn}a_{mn}\delta_{ij}\right) + \left[C_{3a} - C_{3b}\left(a_{ij}a_{ij}\right)^{0.5}\right]kS_{ij} + C_4k\left(a_{ik}S_{jk} + a_{jk}S_{ik} - \frac{2}{3}a_{mn}S_{mn}\delta_{ij}\right) + C_5\left(a_{ik}W_{jk} + a_{jk}W_{ik}\right) \quad (17)$$

In Eq. (17), a_{ij}, S_{ij} and W_{ij} are components of the anisotropy, strain rate and rotation rate tensors, respectively. The bubble-induced turbulence source term was calculated using Eq. (14) and then split amongst the normal Reynolds stress components following Colombo et al. (2015):

$$S_{ij}^{BI} = \begin{bmatrix} 1.0 & 0.0 & 0.0 \\ 0.0 & 0.5 & 0.0 \\ 0.0 & 0.0 & 0.5 \end{bmatrix} S_k^{BI} \quad (18)$$

Values of the coefficients used for the k-ε model and the RSM can be found in Table 2.

Table 2. Coefficients of the turbulence models.

***k*-ε**	$\sigma_k = 1.0$; $\sigma_\varepsilon = 1.3$; $C_{1\varepsilon} = 1.44$; $C_{2\varepsilon} = 1.92$; $C_\mu = 0.09$
RSM SSG	$C_{1a} = 1.7$; $C_{1b} = 0.9$; $C_2 = 1.05$; $C_{3a} = 0.8$; $C_{3b} = 0.65$; $C_4 = 0.625$; $C_5 = 0.2$

3.2. The S_γ model

The S_γ model (Lo and Rao, 2007; Lo and Zhang, 2009) was used to model the evolution of the bubble population following break-up and coalescence events. In the S_γ model, the bubble size distribution is assumed to obey to a pre-defined log-normal probability distribution $P(d_B)$. Therefore, it is not necessary to divide the bubble size spectrum into a large number of bubble

315 classes, but the bubble population can be characterized from a limited number of parameters, S_γ,
316 related to the moments of the bubble size distribution M_γ:
317

$$S_\gamma = nM_\gamma = n\int_0^\infty d_B^\gamma P(d_B)\, d(d_B) \tag{19}$$

318
319 where n is the bubble number density. The zero[th] order moment is equal to the bubble number
320 density n, whereas S_2 and S_3 are closely related to the interfacial area concentration a_i and to the
321 void fraction:
322

$$S_0 = n;\ S_2 = n\int_0^\infty d_B^2 P(d_B)\, d(d_B) = \frac{a_i}{\pi};\ S_3 = n\int_0^\infty d_B^3 P(d_B)\, d(d_B) = \frac{6\alpha}{\pi} \tag{20}$$

323
324 From a knowledge of S_2 and S_3, the average bubble diameter can be determined by using the
325 definition of the Sauter mean diameter (SMD):
326

$$d_{SM} = d_{32} = \frac{S_3}{S_2} = \frac{6\alpha}{a_i} \tag{21}$$

327
328 In addition, the variance of the distribution can also be calculated:
329

$$\sigma^2 = \ln\left(\frac{d_{32}}{d_{30}}\right) = \ln\left[\frac{(S_3/S_2)}{(S_3/S_0)^{1/3}}\right] \tag{22}$$

330
331 The two average diameters, d_{32} and d_{30}, are equal only in presence of a homogeneous distribution.
332 Once the model is combined with a two-fluid Eulerian–Eulerian model that solves for the void
333 fraction, S_3 is known, and only two additional moments, namely S_0 and S_2, are sufficient to

characterize the bubble size distribution. For each moment, a transport equation of the following type needs to be solved:

$$\frac{\partial S_\gamma}{\partial t} + \nabla \cdot \left(S_\gamma \boldsymbol{U}_a\right) = S_{br}^{\gamma} + S_{cl}^{\gamma} \tag{23}$$

In this equation, the velocity of the air $\boldsymbol{U_a}$ is given by the two-fluid model and S^{γ}_{br} and S^{γ}_{cl} are source terms that account for bubble break-up and coalescence in the γ^{th} moment equation. Amongst the different mechanisms, interactions induced by turbulence were assumed to be dominant (Lo and Zhang, 2009; Yao and Morel, 2004) and the only sources of break-up and coalescence in Eq. (23).

The source term for bubble break-up is expressed as:

$$S_{br}^{\gamma} = \int_0^{\infty} K_{br} \Delta S_{\gamma}^{br} n P(d_B) d(d_B) \tag{24}$$

Here, K_{br} is the break-up rate, which is the reciprocal of the break-up time τ_{br}. ΔS_{γ}^{br} is the change in S_γ due to a single break-up event, which, from conservation of volume, is:

$$\Delta S_{\gamma}^{br} = d_B^{\gamma}\left(N_f^{\frac{3-\gamma}{\gamma}} - 1\right) \tag{25}$$

The number of daughter bubbles N_f was assumed equal to 2 (Lo and Zhang, 2009; Luo and Svendsen, 1996; Yao and Morel, 2004). The break-up source term then becomes:

$$S_{br}^{\gamma} = \int_0^{\infty} \frac{d_B^{\gamma}\left(N_f^{3-\gamma/3} - 1\right)}{\tau_{br}} n P(d_B) d(d_B) \tag{26}$$

353

354 The break-up timescale follows from the frequency of the second oscillation mode of a droplet (Lo
355 and Zhang, 2009):

356

$$\tau_{br} = 2\pi k_{br}\sqrt{\frac{3\rho_d + 2\rho_c}{192\sigma}d_B^3} \tag{27}$$

357

358 where k_{br}=0.2, the subscript d identifies the dispersed phase and σ is the surface tension. The break-
359 up criterion was expressed as a function of a critical Weber number We_{cr}, therefore a bubble breaks
360 when the Weber number is higher than the critical value:

361

$$d_{cr} = (1 + C_\alpha)\left(\frac{2\sigma We_{cr}}{\rho_c}\right)^{3/5}\varepsilon^{-2/5} \tag{28}$$

362

363 C_α, equal to 4.6, is a correction factor that accounts for nearby bubbles that disrupt the influence of
364 the surrounding inertial forces. In Lo and Zhang (2009), We_{cr} = 0.31, whilst in Yao and Morel
365 (2004), We_{cr} = 1.24.

366

367 The general source term for bubble coalescence is:

368

$$S_{cl}^{\gamma} = \int_0^\infty \int_0^\infty K_{cl}^{d,d\prime}\Delta S_{\gamma,cl}^{d_B,d_B'} n^2 P(d_B')d(d_B')P(d_B)d(d_B) \tag{29}$$

369

370 Here, $K_{cl}^{d,d\prime}$ is the coalescence rate between two bubbles with diameters d_B and d_B', and $\Delta S_{\gamma,cl}^{d_B,d_B'}$ is
371 the change in S_γ due to a single coalescence event. To avoid excessive complication, a uniform

372 bubble distribution with an equivalent mean diameter d_{eq} was assumed when computing the change
373 in S_γ due to a single coalescence event (Lo and Zhang, 2009):
374

$$\Delta S_{\gamma,cl}^{d,d\prime} = d_{eq}^{\gamma}\left(2^{\gamma/3} - 2\right) \tag{30}$$

375
376 The coalescence rate is expressed as:
377

$$K_{cl}^{d,d\prime} = F_{cl} k_{cl} d_{eq}^2 u_r P_{cl} \tag{31}$$

378
379 Following Chester (1991), Lo and Zhang (2009) considered two different coalescence mechanisms
380 resulting from viscous and inertial collisions. For viscous coalescence, the film drainage model was
381 applied for the coalescence probability (Prince and Blanch, 1990). When two bubbles collide, they
382 trap a thin liquid film between them that prevents coalescence. If the interaction time in the
383 turbulent flow is sufficient for the film to drain out until rupture of the film occurs, then the bubbles
384 coalesce, otherwise the bubbles are separated and coalescence does not occur. The drainage time
385 was calculated from a model for a partially mobile interface and a quasi-steady flow in the film (Lo
386 and Zhang, 2009):
387

$$t_d = \frac{\pi \mu_d \sqrt{F_i}}{2 h_{cr}} \left(\frac{d_{eq}}{4\pi\sigma} \right) \tag{32}$$

388
389 Here, F_i is the interaction force during collision and h_{cr} the critical film thickness (Lo and Zhang,
390 2009). The coalescence probability is then expressed from the interaction time t_i and the drainage
391 time t_d:
392

$$P_{cl} = exp(-t_d/t_i) = exp(t_d\dot{\gamma}) \quad (33)$$

393

394 where the interaction time is the inverse of the Kolmogorov shear rate:

395

$$\dot{\gamma} = \sqrt{\frac{\varepsilon\rho_c}{\mu_c}} \quad (34)$$

396

397 Finally, in Eq. (31), k_{cl} = $(8\pi/3)^{0.5}$ and the relative velocity between the bubbles u_r = $\dot{\gamma}d_{eq}$.
398 Alternatively, for inertial collision, k_{cl} = $(2\pi/15)^{0.5}$ and u_r = $(\varepsilon d_{eq})^{1/3}$. With regard to the probability
399 of coalescence, the major role is played by bubble shape oscillations and, therefore, the coalescence
400 probability was expressed following Chester (1988):

401

$$P_{cl} = \frac{\Phi_{max}}{\pi}\left[1 - \frac{k_{cl,2}^2(We - We_0)^2}{\Phi_{max}^2}\right]^{1/2} \quad (35)$$

402

403 where Φ_{max} is the maximum phase difference (Lo and Zhang, 2009), $k_{cl,2}$ = 12.7, We_0 = $0.8We_{cr}$ and
404 h_0 = $8.3h_{cr}$.

405

406 A different coalescence model, proposed by Yao and Morel (2004), was also considered in this
407 work. When using the Yao and Morel (2004) approach, the break-up model described above was
408 retained, except for the value of We_{crit} which was modified to 1.24, following the authors' proposal.
409 In Yao and Morel (2004), the number of coalescence events per unit volume and unit time, which is
410 assumed to be mainly due to the collisions induced by turbulence, is expressed as:

411

$$K_{cl}^{d,d'}n^2 = -C_1\frac{\varepsilon^{1/3}\alpha^2}{d_{SM}^{11/3}}\frac{1}{g(\alpha) + C_2\sqrt{We/We_{crit}}}exp\left(-C_3\sqrt{We/_{We_{crit}}}\right) \quad (36)$$

412

413 The first part of this equation represents the collision rate between the bubbles, whilst the
414 exponential function describes the probability of coalescence following a collision event. The
415 function $g(\alpha)$ accounts for the effect of the packing of the bubbles when the void fraction is higher
416 than a certain value. From Yao and Morel (2004), C_1 = 2.86, C_2 = 1.922, C_3 = 1.017 and We_{crit} =
417 1.24.

418

419 When two groups of bubbles were included, additional source terms were added to the mass and
420 momentum conservation equations to account for the exchanges between the groups. In a similar
421 manner as above, the conservation equation for the moment of the bubble size distribution becomes:

422

$$\frac{\partial S_{\gamma,n}}{\partial t} + \nabla \cdot \left(S_{\gamma,n}\boldsymbol{U}_{a,n}\right) = S^{\gamma}_{br,n} + S^{\gamma}_{cl,n} + D^{\gamma}_{br,n} + B^{\gamma}_{cl,n} + B^{\gamma}_{br,n} + D^{\gamma}_{cl,n} \tag{37}$$

423

424 In this equation, the subscript n identifies the bubble group and assumes the values s for spherical
425 bubbles and c for cap bubbles. D^{γ}_{br} and D^{γ}_{cl} are source terms for the death of bubbles by break-up to
426 the previous group and by coalescence to the following group. Conversely, B^{γ}_{br} and B^{γ}_{cl} are due to
427 the birth of bubbles by coalescence from the previous group and by break-up from the following
428 group. Obviously, when only two groups are considered, Eq. (37) simplifies and the only source
429 terms to be considered are the death of cap bubbles which gives rise to the birth of spherical bubbles
430 by break-up, and the death of spherical bubbles with the birth of cap bubbles by coalescence.

431

432 In this work, break-up of cap bubbles into spherical bubbles has been neglected, with this
433 assumption explained and justified in detail in the results section. To calculate the additional
434 sources accounting for exchanges between groups, using Eq. (29), Eq. (30) and the hypothesis of a

435 uniform bubble distribution for the coalescence source, the source terms for the death of spherical
436 bubbles by coalescence are obtained as:
437

$$D_{cl,s}^{0} = -2 \cdot \left(K_{cl,s}^{d,d'} n_s^2\right) f(d_B) \tag{38}$$

438

$$D_{cl,s}^{2} = -2 d_{eq}^{2} \left(K_{cl,s}^{d,d'} n_s^2\right) f(d_B) \tag{39}$$

439

440 $f(d_B)$ is a function that expresses the probability that a coalescence event between two spherical
441 bubbles leads to the birth of a cap bubble. Therefore, it is the ratio of the number of coalescence
442 events that generate a cap bubble to the total number of coalescence events amongst the spherical
443 bubble population. The coefficients -2 and $-2d^2_{eq}$ are calculated from the second contribution to Eq.
444 (30) and reflect the fact that, in these events, the results is not a net change in the value of S_γ for the
445 spherical bubbles, but a loss of two bubbles and their interfacial area to the cap bubbles.
446 Accordingly, from the first contribution to Eq. (30), the gain in S_γ in the cap bubble group due to
447 coalescence events in the spherical bubble group is obtained as:
448

$$B_{cl,c}^{0} = \left(K_{cl,c}^{d,d'} n_c^2\right) f(d_B) \tag{40}$$

449

$$B_{cl,c}^{2} = 1.59 \cdot d_{eq}^{2} \left(K_{cl,c}^{d,d'} n_c^2\right) f(d_B) \tag{41}$$

450

451 From Eq. (38), the mass source from spherical to cap bubbles can be obtained, using the volume
452 average bubble diameter:
453

$$\Gamma_{sc} = -\Gamma_{cs} = -D_{cl,s}^{0} \frac{\pi d_{30,s}^{3}}{6} \rho_a \tag{42}$$

454

455 Finally, for simplicity, the function $f(d_B)$ was assumed equal to ratio of the SMD to the critical
456 diameter:

457

$$f(d_B) = \frac{d_{SM}}{d_c} \tag{43}$$

458

459 In the previous equation, d_c is the critical diameter at which bubble behaviour changes from a
460 spherical bubble to a cap bubble.

461

462 The overall model, implemented in the STAR-CCM+ CFD code (CD-adapco, 2014), was solved in
463 a two-dimensional axisymmetric geometry. At the inlet, fully-developed phase velocities and void
464 fraction boundary conditions were imposed, together with an imposed pressure at the outlet and the
465 no-slip condition at the wall. Experimental measurements of average bubble diameter at the first
466 measurement station were used for the bubble diameter inlet boundary condition. Therefore,
467 experimental measurements at the last station were compared against predictions at a distance from
468 the inlet equal to that between the first and the last measurement stations. Strict convergence of
469 residuals was ensured, together with a mass balance error lower than 0.01 % for both phases.
470 Experiment HI2 was selected for a mesh sensitivity study, the results of which are presented in
471 Figure 1 in terms of the radial profiles of water velocity, turbulence kinetic energy, void fraction
472 and SMD. The radial profiles are shown as a function of the normalized radial position *r/R*, which is
473 equal to 0 at the pipe centre and to 1 at the pipe wall. Four grids were tested with a progressively
474 increasing number of equidistant grid nodes (10 × 100, 15 × 150, 20 × 200, and 25 × 250). The
475 water velocity and void fraction distributions are rather insensitive to the number of nodes, but
476 some differences between the various grids are apparent for the turbulence kinetic energy and the
477 SMD. From the results in Figure 1, the grid with 20 × 200 nodes was chosen for other simulations.

All grids had a first grid node higher than, but close, to $y^+ = 30$, which is the lower limit for the use of wall functions.

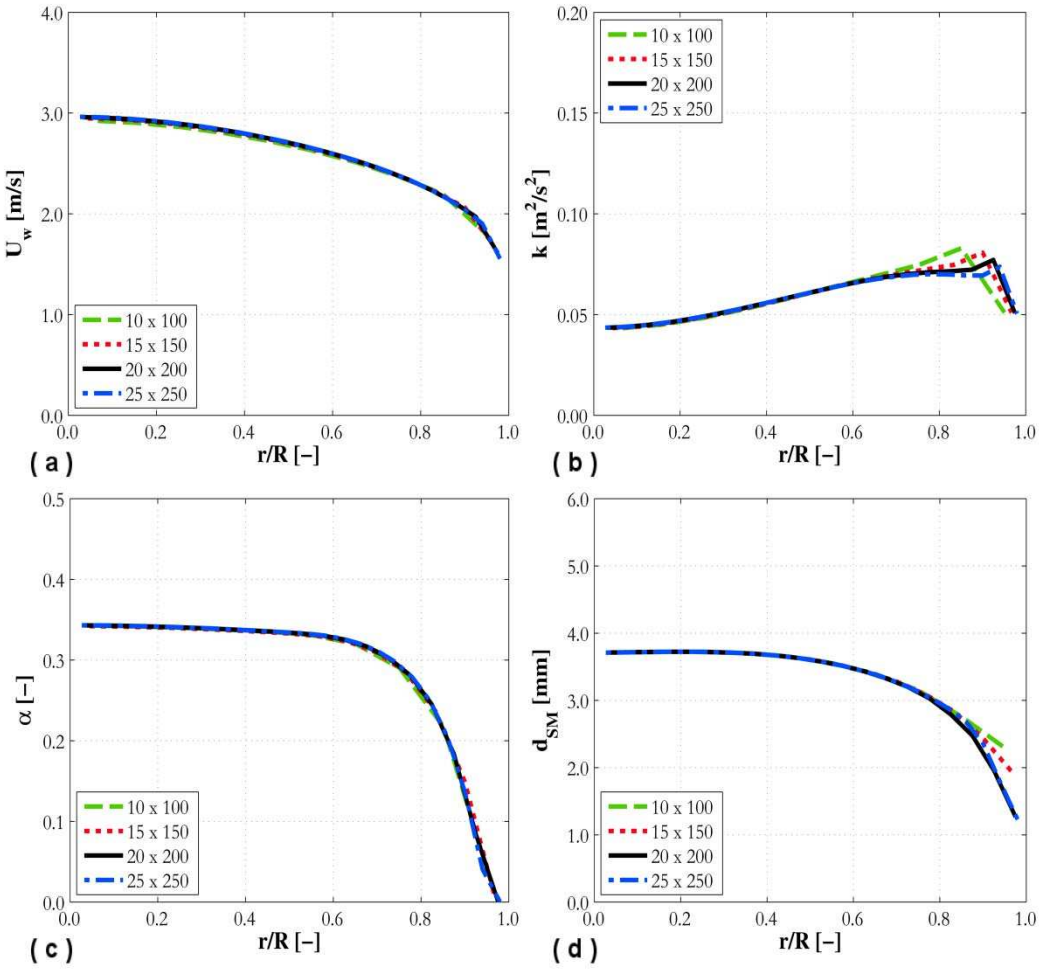

Figure 1. Mesh sensitivity study in terms of radial and axial node numbers for experiment HI2. Water velocity (a), turbulence kinetic energy (b), void fraction (c) and SMD (d) radial profiles are presented.

4. Results and discussion

This section describes and discusses the simulation results and comparisons against experimental data. First, the experiments of Liu (1993), Hibiki and Ishii (1999) and Hibiki et al. (2001) were simulated with the YM model (Yao and Morel, 2004) and the results are presented in Figure 2 and Figure 3. As can be seen, the YM model generally overestimates the average bubble diameter. In particular, marked overestimations were obtained at the lowest liquid velocities (Hi1, HI1 and L1), whereas, at higher velocities (Hi2, HI2 and L2), the overestimation is reduced and, for experiment

494 HI2 (Figure 3a) only, good agreement with data is found. The tendency of the YM model to over-
495 predict the bubble diameter has already been noted by Cheung et al. (2007) and Nguyen et al.
496 (2013). To serve as a benchmark, predictions from the LZ model (Lo and Zhang, 2009) are also
497 included in Figure 2 and Figure 3. Overall, the LZ model provides better accuracy when predicting
498 the average bubble diameter. Nevertheless, and similar to YM, a strong dependency on the liquid
499 velocity is apparent. At low velocity, good agreement, or limited overestimation of the bubble
500 diameter, was obtained (with respect to YM) but, at higher velocities, LZ under predicts the
501 experiments. In addition, as already reported in Lo and Zhang (2009), the bubble diameter is
502 generally under predicted in the near wall region, probably as a consequence of the excessively
503 strong bubble break-up rate there.
504
505 The availability of experimental data allowed a further optimization of the YM model to be made.
506 As the over prediction of the bubble diameter is possibly due to an excessive amount of bubble
507 coalescence in the flow, this was limited by modifying the value of We_{crit} in Eq. (36), where it
508 mainly impacts the coalescence probability. Therefore, a lower We_{crit} reduces the coalescence
509 probability or, from a different perspective, it reduces the interaction time available to the liquid
510 film trapped between the two colliding bubbles to drain out. Calibration of the model was limited to
511 the coalescence model (the model for break-up was not changed from that of Lo and Zhang (2009),
512 except for the value of We_{crit}, equal to 1.24 for YM). Even if the average bubble diameter is still
513 overestimated at low liquid velocity and underestimated at high liquid velocity, acceptable
514 agreement was achieved in all the tested conditions with $We_{crit} = 0.10$ (YM opt. lines in Figure 2
515 and Figure 3). Overall, the improvement in the accuracy with respect to the original YM and LZ
516 models is significant. In the near wall region, where LZ significantly under predicts the
517 experimental data, the value of the bubble diameter is well predicted, with the exception of
518 experiment HI1 (Figure 2g) in which the flow rate is particularly low. In addition, for the LZ model,
519 optimization on a case-by-case basis has been found necessary to reach a comparable accuracy (Lo

520 and Zhang, 2009), whereas, in this work, the same value of We_{crit} was maintained for all flow
521 conditions considered. In view of this finding, additional research work is required to develop more
522 general and accurate models of bubble break-up and coalescence.
523
524 Figure 2 and Figure 3 also show radial profiles of the mean water velocity and void fraction (for L1
525 and L2, Figure 3e and Figure 3h, the air velocity is also provided). Overall, simulation results are in
526 good agreement with the experiments. The mean velocity is under predicted for L2 and, but only in
527 the pipe core region, for Hi1. With regards to the void fraction, the best agreement is found for the
528 wall-peaked void profiles (Figure 2c, Figure 3f and Figure 3i). In contrast, the core-peaked void
529 profiles were more difficult to predict. As it is possible to see from Figure 2 and Figure 3, a larger
530 bubble size spectrum characterizes the core-peaked void profiles (Hi2, HI1 and HI2) with respect to
531 the wall-peaked profiles, where the average bubble diameter radial distribution is generally flatter.
532 This complicates the simulation of the momentum transfer at the interphase, even with the use of a
533 population balance model. As shown in Figure 2f, Figure 2i and Figure 3c, a sharp increase in the
534 near wall region, followed by an almost flat profile, is usually predicted. The experiments, however,
535 show a more gentle but continuous increase of the void fraction towards the pipe centre. Predictions
536 are similar amongst the three different models considered. This suggests that it is the interphase
537 momentum forces (lift and wall forces in particular) that mostly determine the radial void fraction
538 and mean velocity profiles. In this regard, the use of constant lift force coefficients, not dependent
539 on the bubble diameter, may significantly inhibit changes in the lift force induced by changes in the
540 latter diameter.
541
542 The role of the critical Weber number in the YM model is the focus of the results given in Figure 4,
543 where the average bubble diameter profile is shown for three different values of We_{crit}. It has
544 already been mentioned how We_{crit} mainly affects the coalescence probability. Specifically, a lower
545 We_{crit} reduces the coalescence probability and, therefore, the average bubble diameter. This effect is

546 equivalent to reducing the interaction time available for the liquid film trapped between two
547 colliding bubbles to drain out, or, equivalently, to increasing the time required by this liquid film to
548 drain out. Figure 4 includes two different experimental datasets. It is observed that the reduction in
549 coalescence with We_{crit} is higher at the low flow rate (Figure 4a), while the effect of a lower We_{crit} is
550 reduced at the higher flow rate (Figure 4b). At high flow rates, therefore, the interaction time is low
551 given the high level of turbulence, and hence the coalescence probability has a correspondingly low
552 value. As a consequence, the amount of decrease achievable by tuning We_{crit} is also low. At low
553 flow rates, in contrast, the coalescence probability is higher due to the longer interaction times that
554 occur in a low level turbulence field, and hence this probability can be significantly affected by a
555 change in the value of We_{crit}.

556
557

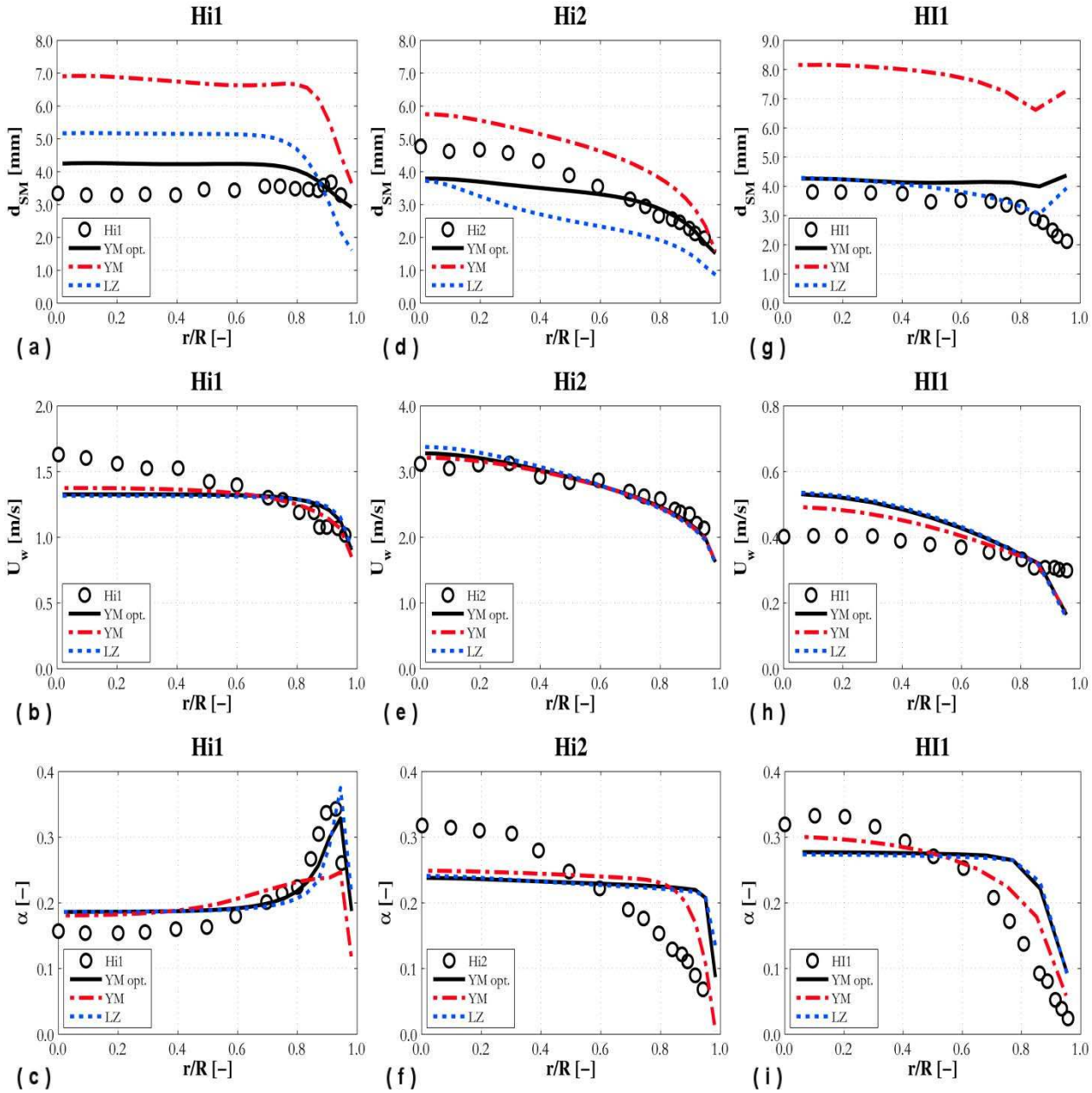

Figure 2. SMD, mean water velocity and void fraction radial profiles compared against experiments Hi1 (a-c), Hi2 (d-f) and HI1 (g-i). Simulation results are shown for LZ (---), YM (-·-) in its standard form (Eq. 36) and after optimization (YM opt., —).

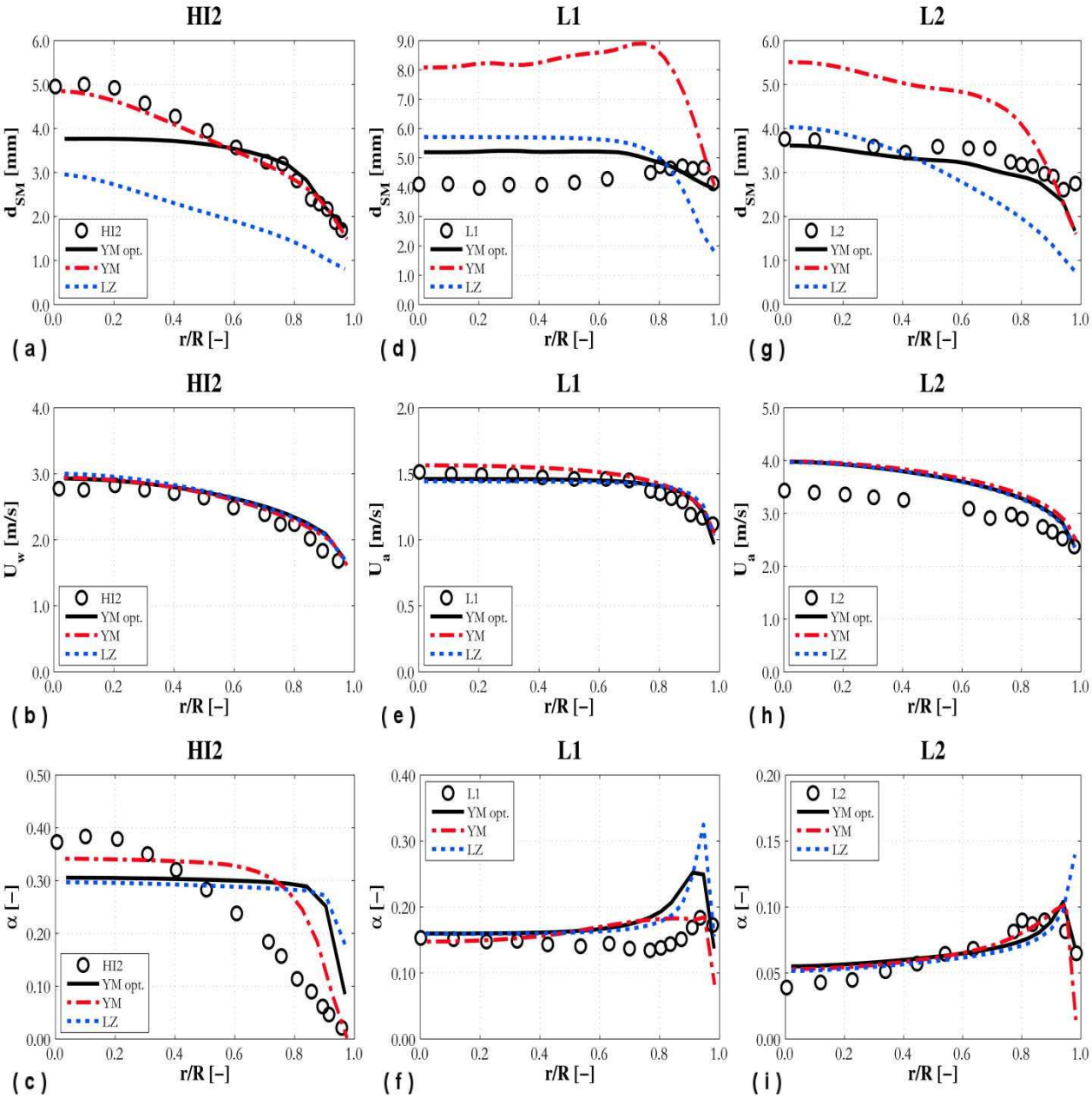

Figure 3. SMD, mean velocity and void fraction radial profiles compared against experiments HI2 (a-c), L1 (d-f) and L2 (g-i). Simulation results are shown for LZ (---), YM (-·-) in its standard form (Eq. 36) and after optimization (YM opt., —).

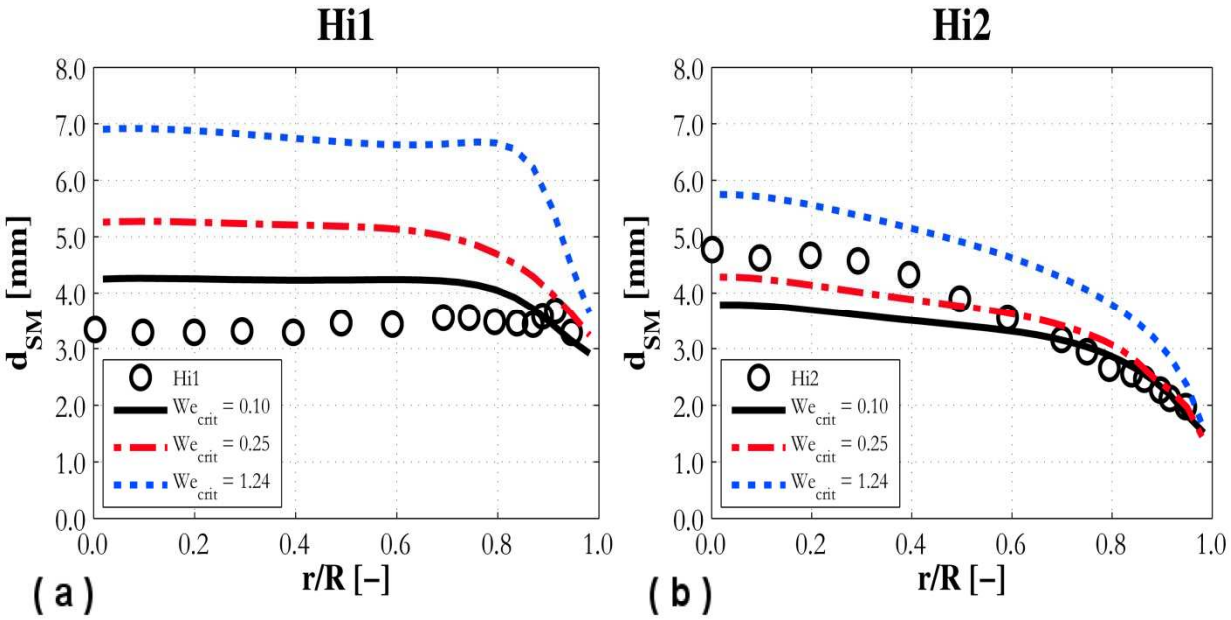

Figure 4. SMD radial profiles obtained with YM and We_{crit} = 0.1 (—), We_{crit} = 0.25 (-·-) and We_{crit} = 1.24 (---). Predictions are compared against experiments Hi1 (a) and Hi2 (b).

4.1. Effect of the break-up model

As mentioned, no changes were introduced in the break-up model, except for the value of the We_{crit}, which, for YM, was increased to 1.24 following the authors' proposal (Yao and Morel, 2004). Since no clear indications of the amount of bubble break-up occurring are available for the flows studied in this work, additional simulations neglecting break-up were made to evaluate the impact of the break-up model on the predictions. In Figure 5, four of the experiments were predicted with and without accounting for break-up. For the majority of the pipe cross-section, the effect of break-up on the bubble diameter distribution is seen to be negligible. In the near wall region, break-up is effective in reducing the average bubble diameter, but only at the highest liquid velocities (Figure 5b and Figure 5d). At low velocities, break-up is negligible even in the region close to the wall (Figure 5a and Figure 5c). Overall, and in view of the agreement obtained with these experiments, these results suggest that coalescence is the dominant mechanism in these flows.

Since only the net result of the combined action of both break-up and coalescence is available in terms of the experimental data, this being the average bubble diameter, additional sensitivity studies

were made, increasing the impact of both. The same We_{crit} value of 0.25 was adopted in both the break-up and the coalescence models. The increase in the rate of coalescence with a higher critical Weber number was already addressed in Figure 4. A lower We_{crit} in the break-up model increases the break-up rate since a lower energy is required to break-up the bubble. The value of We_{crit} adopted is now close to that used in the LZ model and, therefore, a comparable amount of break-up is to be expected. The results are presented in Figure 6. Even if some improvement is obtained for a number of flows (Figure 6a, Figure 6c and Figure 6e), excessive break-up causes an under prediction of bubble diameter at high liquid velocities (Figure 6b, Figure 6d and Figure 6f). In addition, and except for experiment HI1 (Figure 6c), the bubble diameter is always underestimated in the near wall region, where, in view of the higher levels of turbulence, break-up is expected to be more significant. Again, these results are similar to those obtained with the LZ model (Figure 2 and Figure 3), for which an excessive amount of break-up, in particular in the near wall region, has already been reported (Lo and Zhang, 2009). This further supports the case for these flows being coalescence dominated.

Overall, and despite the previous results, it remains difficult to precisely evaluate the accuracy of the model with regard to the competitive action of coalescence and break-up, and the mechanisms involved. As mentioned, only the net result is available through data on the average bubble diameter. Therefore, additional knowledge is required on the physics of these flows, and on the interaction between bubbles and with the continuous phase in particular. The lack of information on these processes is a significant constraint on the further development of these models that needs to be overcome if more accurate modelling is to be achieved. As an example, the recent tendency has been to include all possible mechanisms of bubble break-up and coalescence (e.g. turbulent collision, wake entrainment, shearing-off) (Liao et al., 2015; Smith et al., 2012; Sun et al., 2004). Even if this may benefit the generality of the developed models, the relative influence of each mechanism has been generally optimized with additional constants tuned against average bubble diameter measurements, which, at the present time, is the only real option available to modellers.

Without a clear knowledge of the effective impact of each mechanism as a function of the flow conditions, however, accurate prediction of the average bubble diameter does not guarantee the accuracy of each individual model, and possibly increases the uncertainty in the results and limits the applicability of the model itself. In view of this, advances must rely on the availability of more detailed experimental measurements or, perhaps, accurate direct numerical simulations of bubble behaviour.

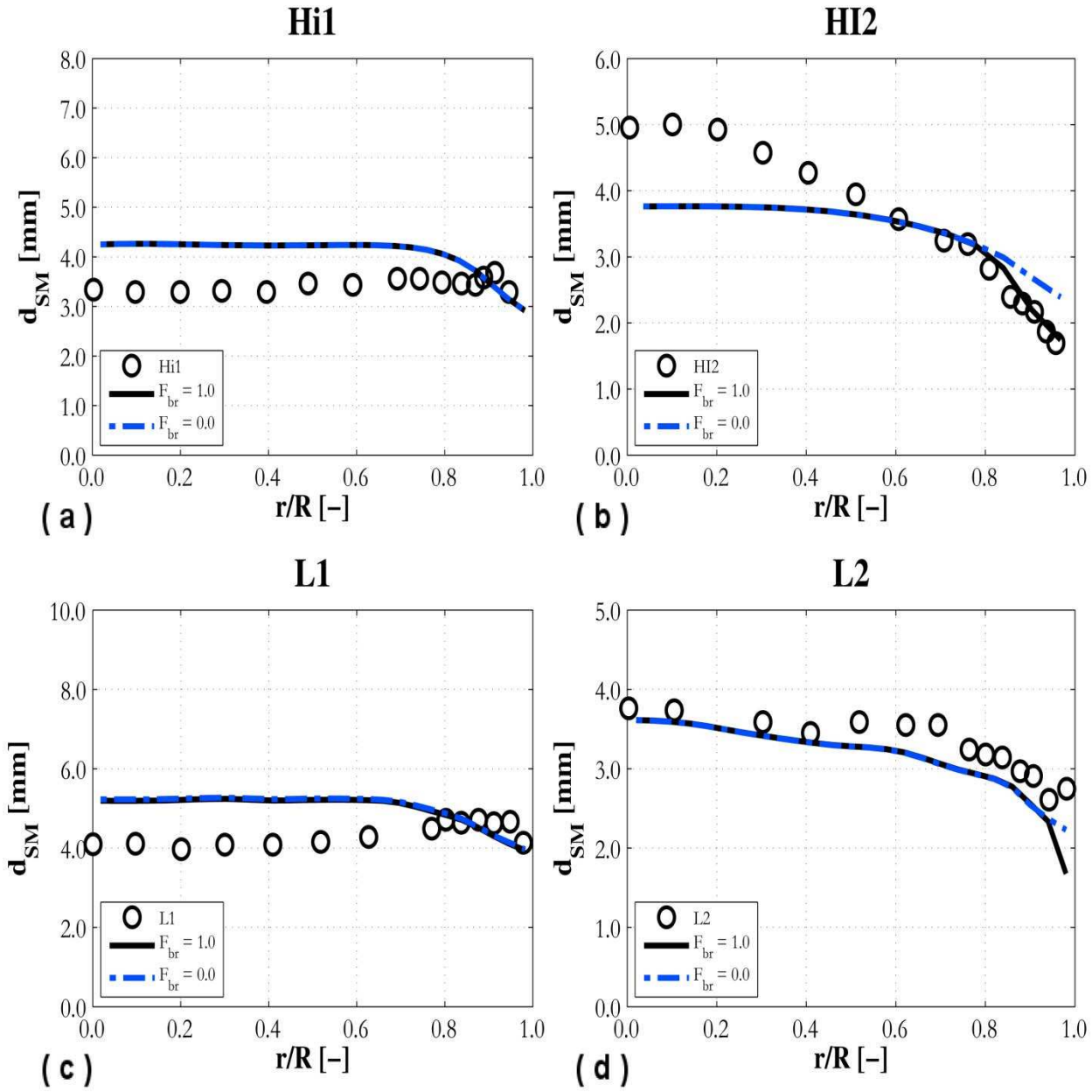

Figure 5. SMD radial profiles with (—) and without (-··-) considering the effect of bubble break-up in the flow. Predictions are compared against experiments Hi1 (a), Hi2 (b), L1 (c) and L2 (d).

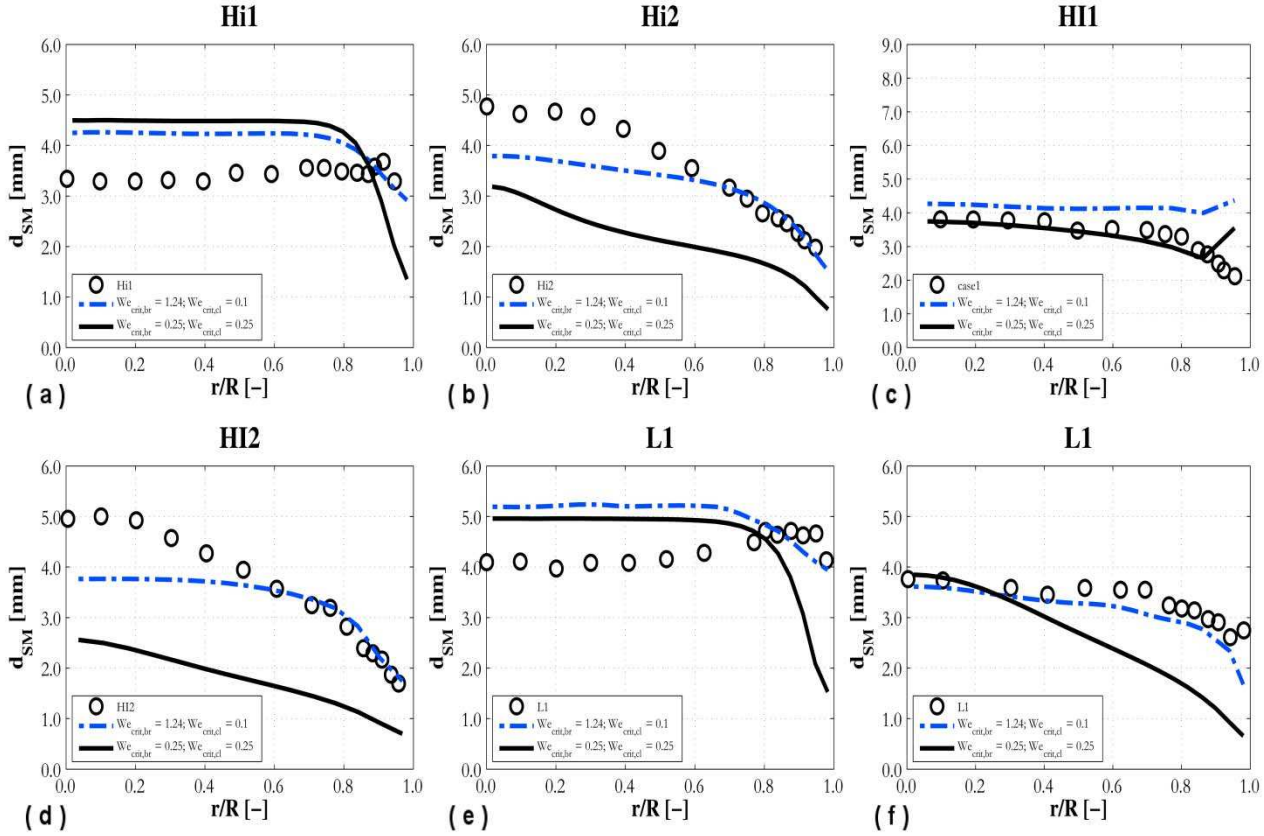

Figure 6. SMD radial profiles at different rates of coalescence and break-up of bubbles in the flow ($We_{crit,br}$ = 1.24 and $We_{crit,cl}$ = 0.1 (—); $We_{crit,br}$ = 0.25 and $We_{crit,cl}$ = 0.25 (-··-)). Predictions are compared against the experiments in Table 1.

4.2. Continuous phase turbulence sensitivity

Turbulence parameters affect in different ways the models for coalescence and break-up, and, as the latter models are based on the collision of bubbles due to turbulence, they are expected to have a significant impact on results. The sensitivity to the turbulence model predictions has already been investigated in some literature studies (Nguyen et al., 2013; Yao and Morel, 2004), but, in many more, the assessment and optimization of the coalescence and break-up models was carried out without considering the accuracy of the turbulence predictions. The aim of this section, therefore, is to address the dependency of results on the continuous phase turbulence.

In bubbly flows, the contribution of the bubbles to the continuous phase turbulence is accounted for, in the *k*-*ε* turbulence model, by source terms in the equations of that model (Eq. (11) and Eq. (12), Section 3.1).

646

647 Figure 7 shows radial profiles of the predicted SMD as a function of the amount of bubble-induced
648 turbulence, together with the continuous phase streamwise turbulence intensities *I*. Turbulence
649 measurements are available only from Hibiki and Ishii (1999) and Hibiki et al. (2001), where
650 turbulence intensity was calculated by dividing the streamwise r.m.s of the velocity fluctuations by
651 the maximum liquid velocity. Three different cases are considered: no bubble-induced turbulence,
652 and Eq. (14) with K_{BI} = 0.25 and K_{BI} = 1.0. At low flow rates (HI1, Figure 7i), or for wall-peaked
653 void profiles (Hi1, Figure 7g, and L1, Figure 7k), where the presence of the bubbles induces a flat
654 mean velocity profile and a strong reduction of the shear-induced turbulence production in the pipe
655 centre, the contribution of the bubble-induced turbulence is significant. For the high flow rate wall-
656 peaked case (L2, Figure 7l), where the turbulence level is already high and the void fraction in the
657 pipe centre is low, and the core-peaked void profiles (Hi2, Figure 7h, and HI2, Figure 7j), where the
658 shear-induced production remains significant, the impact of the bubble-induced contribution is less.
659 In the first case scenario, significant differences in the turbulence level cause bubble diameter
660 profiles to be very different from one another (Figure 7a, Figure 7c and Figure 7e). This means that
661 these results are dependent on the continuous phase turbulence and, for some flows, on the bubble-
662 induced turbulence model as well. Therefore, for a proper model validation, both the average
663 bubble diameter and the continuous phase turbulence predictions need to be compared against
664 experiments. Conversely, the results may be dependent not only on the flows used for validation,
665 but also on the specific bubble-induced turbulence model. Unfortunately, turbulence measurements
666 are not available for all the experiments considered. Moreover, for the data of Hibiki et al. (2001),
667 turbulence levels were always under predicted, even when considering all the drag force to be
668 converted to turbulence kinetic energy. It must be pointed out that the turbulence intensities in these
669 data appear significantly higher than for other experiments in the literature having comparable
670 geometry and flow conditions (Liu, 1998; Serizawa et al., 1975; Wang et al., 1987). For HI1 and
671 HI2, instead, satisfactory predictions were obtained. In view of the limited number of simultaneous

672 measurements of both the bubble diameter distribution and the flow turbulence, some additional
673 comparisons are shown in Figure 8, taking advantage of a previous validation of the bubble-induced
674 turbulence model (Eq. (14) and Eq. (15)), which showed satisfactory accuracy over a wide range of
675 conditions (Colombo and Fairweather, 2015). In Figure 8, radial profiles of the r.m.s. of streamwise
676 velocity fluctuations are compared against different bubbly flow data in vertical pipes. For these
677 validations, the bubble diameter was fixed and assumed equal to experimental observations, even if
678 only rough averaged values were available for the majority of the experiments. Even if some
679 discrepancies are still apparent, the overall agreement can be considered satisfactory. This
680 additional validation, although useful, did not allow a comparison of bubble diameter and
681 turbulence for the same experiment and, therefore, concerns related to data availability still remain.
682 Recently, the development of advanced experimental techniques has allowed detailed
683 measurements of the average bubble diameter and the bubble diameter distribution (Lucas et al.,
684 2005, 2010; Prasser et al., 2007). However, in view of the previous results and to better support the
685 modelling effort, experimental measurements need to allow not only the validation of the bubble
686 diameter distribution, but also of the continuous phase turbulence level.
687
688 In Figure 7, YM predicts a higher SMD, therefore a higher coalescence ratio, with a decrease in the
689 continuous phase turbulence. Collision rate increases with turbulence, while coalescence probability
690 reduces, with the latter being the dominant effect. This qualitatively behaviour needs further
691 examination. In Figure 9, the same sensitivity study is made for the LZ model, for experiments Hi1,
692 Hi2 and L1. The turbulence intensity behaviour remains the same, but the bubble diameter
693 predictions are changed. At low liquid velocity (Hi1 and L1) and without the bubble-induced
694 turbulence model, bubble diameter is high at the wall, where the turbulence remains high, whereas
695 it is low in the centre of the pipe due to the reduced turbulence in this region. When the turbulence
696 level is increased, the coalescence is also increased, and, consequently, the SMD. With a further
697 increase of the turbulence, the bubble diameter is reduced by a decrease of the coalescence or, more

likely, by an increase of bubble break-up, which is higher for this model (Section 4.2). At high velocity (Hi2), the break-up is already high even without including bubble-induced turbulence. Therefore, with an increase of the turbulence level, the break-up is further increased and a decrease of the SMD is observed. For YM, even if a reduction in the coalescence following an increase of the turbulence, at already high turbulence levels, cannot be excluded, in the limit of zero turbulence, an increase of the coalescence is expected following an increase in the turbulence. Therefore, despite the good accuracy shown, the qualitative behaviour of YM with the turbulence level, which is different from that of LZ, suggests the need for additional future verification of these models.

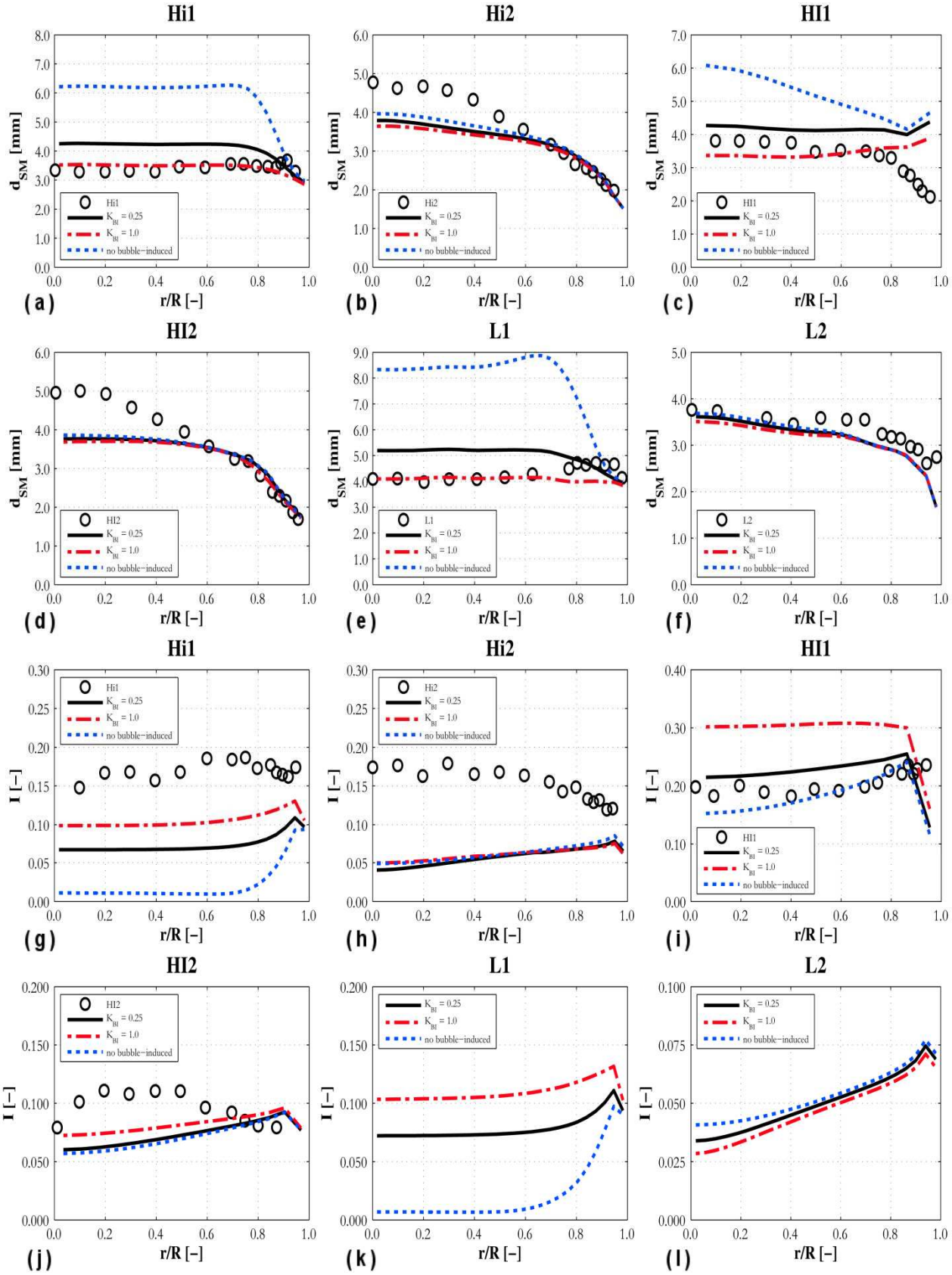

Figure 7. SMD (a-f) and turbulence intensity (g-l) radial profiles without bubble-induced turbulence (---), and with bubble-induced turbulence, and for K_{BI} = 0.25 (—) and K_{BI} = 1.0 (-·-). Predictions, obtained with YM and We_{crit} = 0.1, are compared against experiments in Table 1.

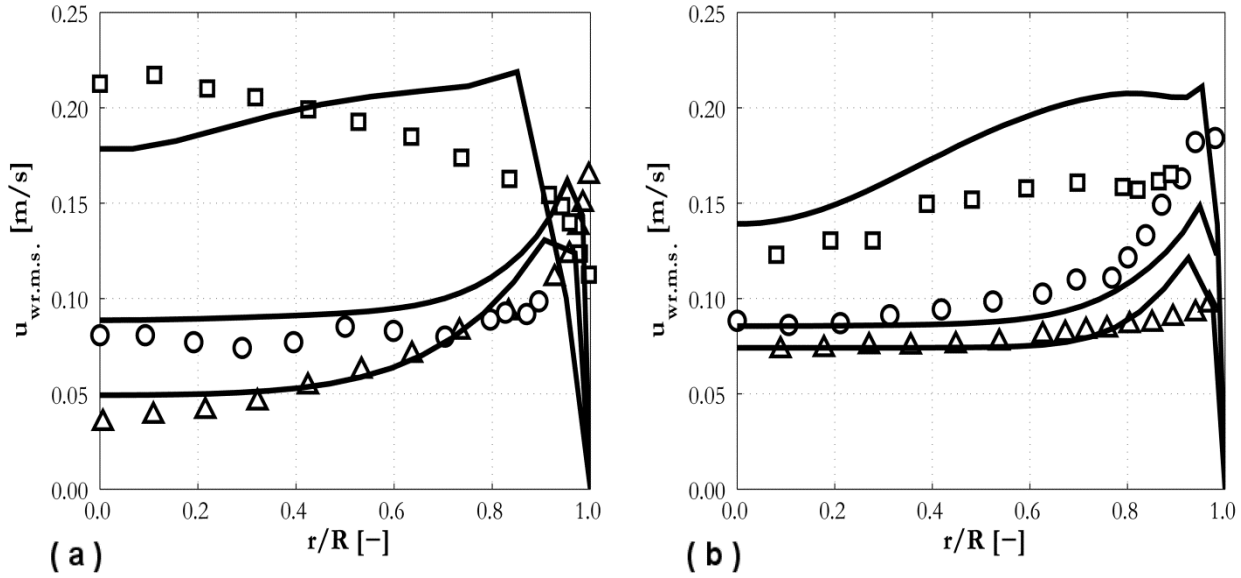

Figure 8. Radial profiles of r.m.s. of streamwise velocity fluctuations compared against experiments in bubbly pipe flows (Colombo and Fairweather, 2015). (a) Liu and Bankoff (1993), j_w = 1.087 m/s, j_a = 0.112 m/s (Δ); Serizawa et al. (1975), j_w = 1.03 m/s, j_a = 0.291 m/s (○); Liu and Bankoff (1993), j_w = 0.376 m/s, j_a = 0.347 m/s (□). (b) Wang et al. (1987), j_w = 0.71 m/s, j_a = 0.1 m/s (Δ); Liu (1998), j_w = 1.0 m/s, j_a = 0.22 m/s (○); Serizawa et al. (1975), j_w = 1.03 m/s, j_a = 0.436 m/s (□).

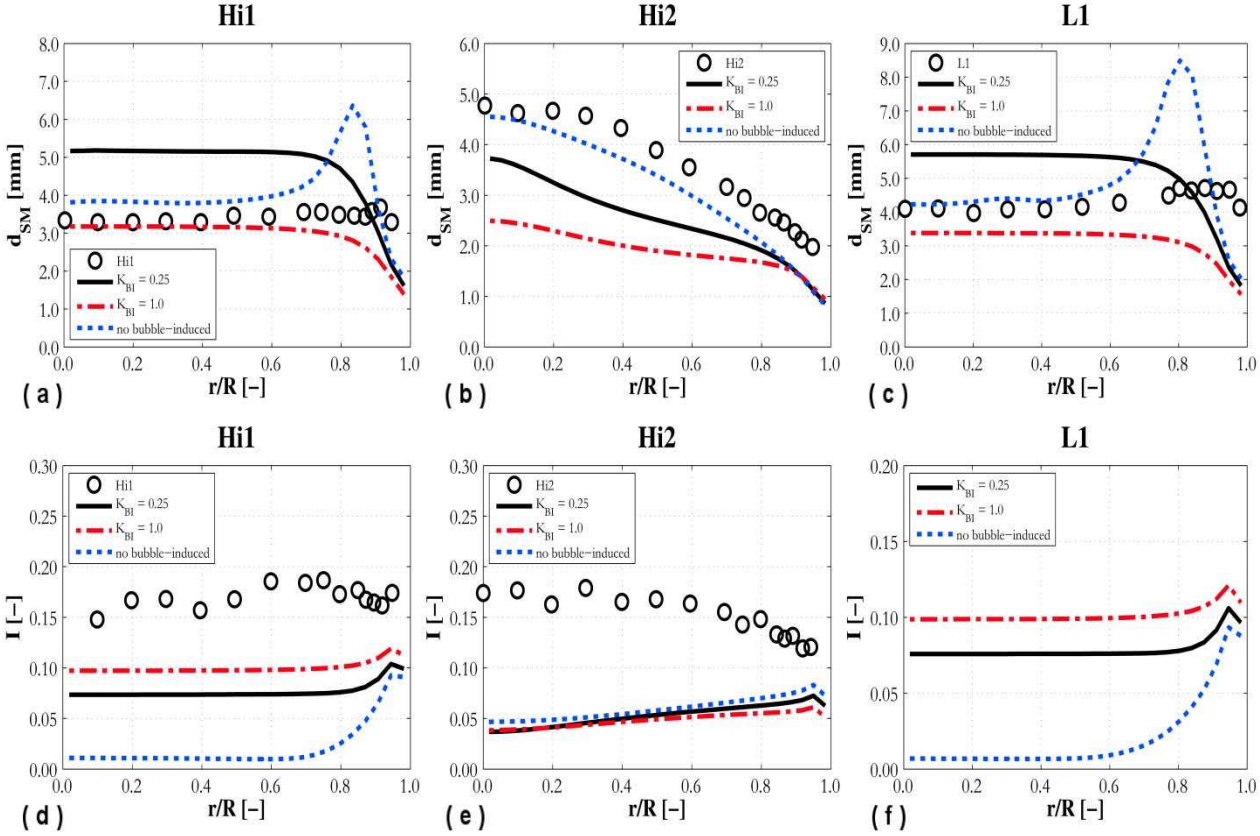

Figure 9. SMD (a-c) and turbulence intensity (d-f) radial profiles without bubble-induced turbulence (---), and with bubble induced turbulence, and for K_{BI} = 0.25 (—) and K_{BI} = 1.0 (-··-). Predictions, obtained with LZ, are compared against experiments Hi1 (a,d), Hi2 (b,e) and L1 (c,f).

4.3. Reynolds stress turbulence model

Using the YM model, the same tests were repeated with a Reynolds stress turbulence model and the results are presented in Figure 10 and Figure 11. A comparable level of agreement with data is found using both turbulence models for the SMD profiles (Figure 10 a-c and Figure 11 a-c), and similar velocity profiles were obtained (Figure 10 d-f and Figure 11 d-f). Similar void fraction profiles were also obtained for the wall-peaked cases (Figure 10g, Figure 11h and Figure 11i), although for the core-peaked profiles, the behaviour of the void fraction is reproduced better by the RSM (Figure 10h, Figure 10i and Figure 11g). More specifically, in such cases the void fraction gently increases from the wall towards the pipe centre. However, for the k-ε model, the increase is sharper near the wall, and the profile is then flatter towards the pipe centre. In a turbulent bubbly flow, the turbulence may interact with the interphase forces, inducing a radial pressure gradient in the flow that impacts upon the distribution of the dispersed phase (Ullrich et al., 2014). Generally, since the turbulence is higher near the wall, the pressure accordingly increases towards the pipe centre. It is this pressure gradient that is likely responsible for the over predicted void fraction peak for experiment L2 (Figure 11i).

In bubbly pipe flows, the turbulence is anisotropic, and this anisotropy can be reproduced using a Reynolds stress model (Colombo et al., 2015). Therefore, different results should be expected when using a k-ε model, because of the different turbulent stresses, or if the turbulence kinetic energy is added to the pressure. It must be noted, however, that differences between the two turbulence modelling approaches might be obscured by the influence of the interfacial momentum forces, which have been the object of a significant amount of optimization and refinement in the past. It is the opinion of the authors, however, that even when a similar accuracy is obtained (wall-peaked profiles), the use of a Reynolds stress formulation provides more insight into the distinctive features of the flow and should assist the development of models of more general applicability. In this

749 regard, Ullrich et al. (2014) predicted some wall-peaked void fraction profiles with an RSM, whilst
750 neglecting lift and wall reflection forces.
751
752 Differences between the turbulence model predictions are also apparent in the turbulence intensity
753 profiles (Figure 10 j-l and Figure 11 j-l). These, even if small for the majority of cases, induce
754 differences in the coalescence rates which, as discussed in the previous section, are strongly
755 dependent on the turbulence in the continuous phase. The different coalescence rates, together with
756 differences in the void fraction profiles, can be considered the reason for the slight disparity in the
757 bubble diameter and the mean velocity profiles between the k-ε model and the RSM.
758
759

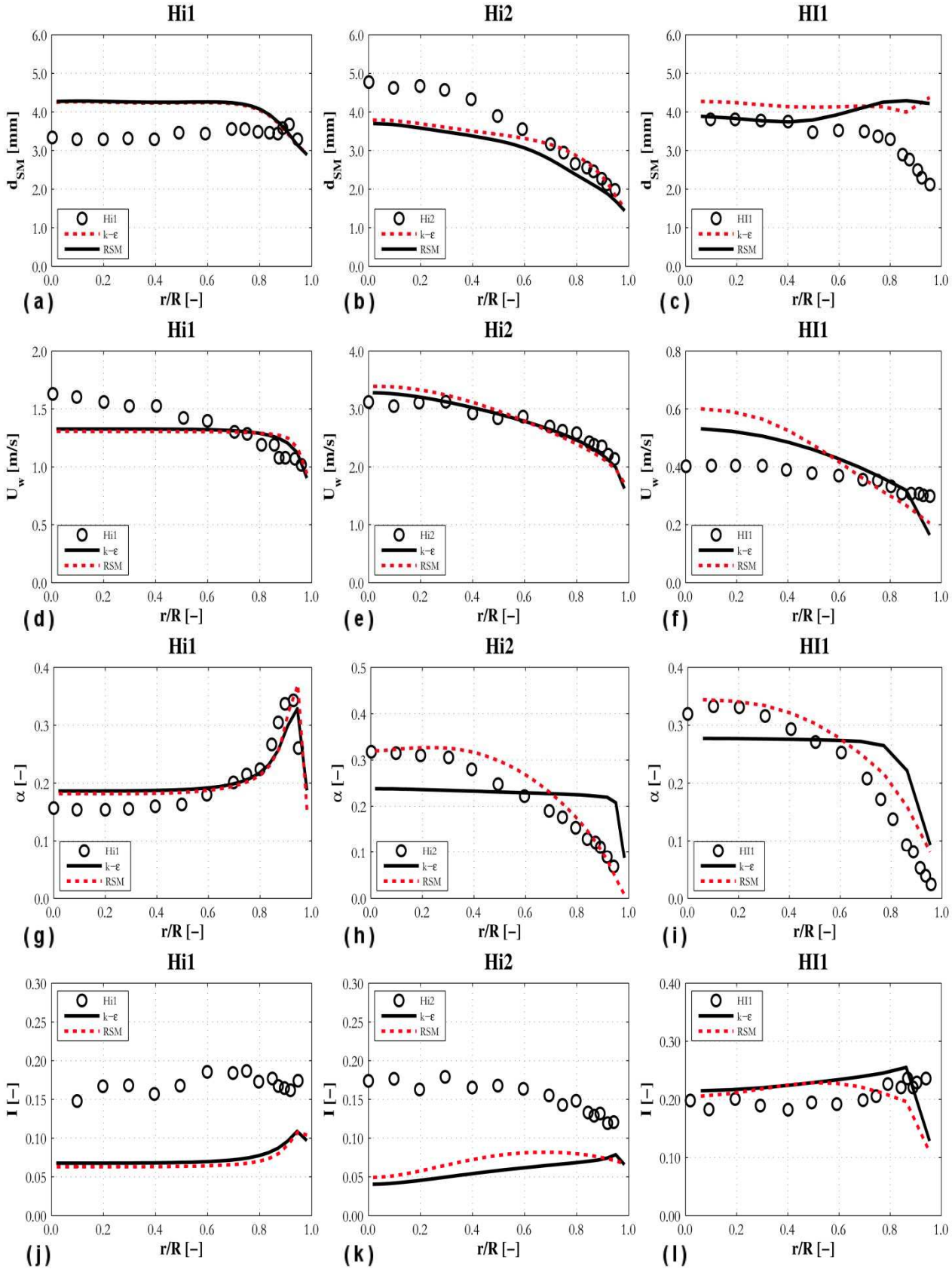

Figure 10. SMD (a-c), mean velocity (d-f), void fraction (g-i) and turbulence intensity (j-l) radial profiles compared against experiments Hi1, Hi2 and HI1. Predictions were obtained with a *k-ε* (—) and a Reynolds stress (---) turbulence formulation.

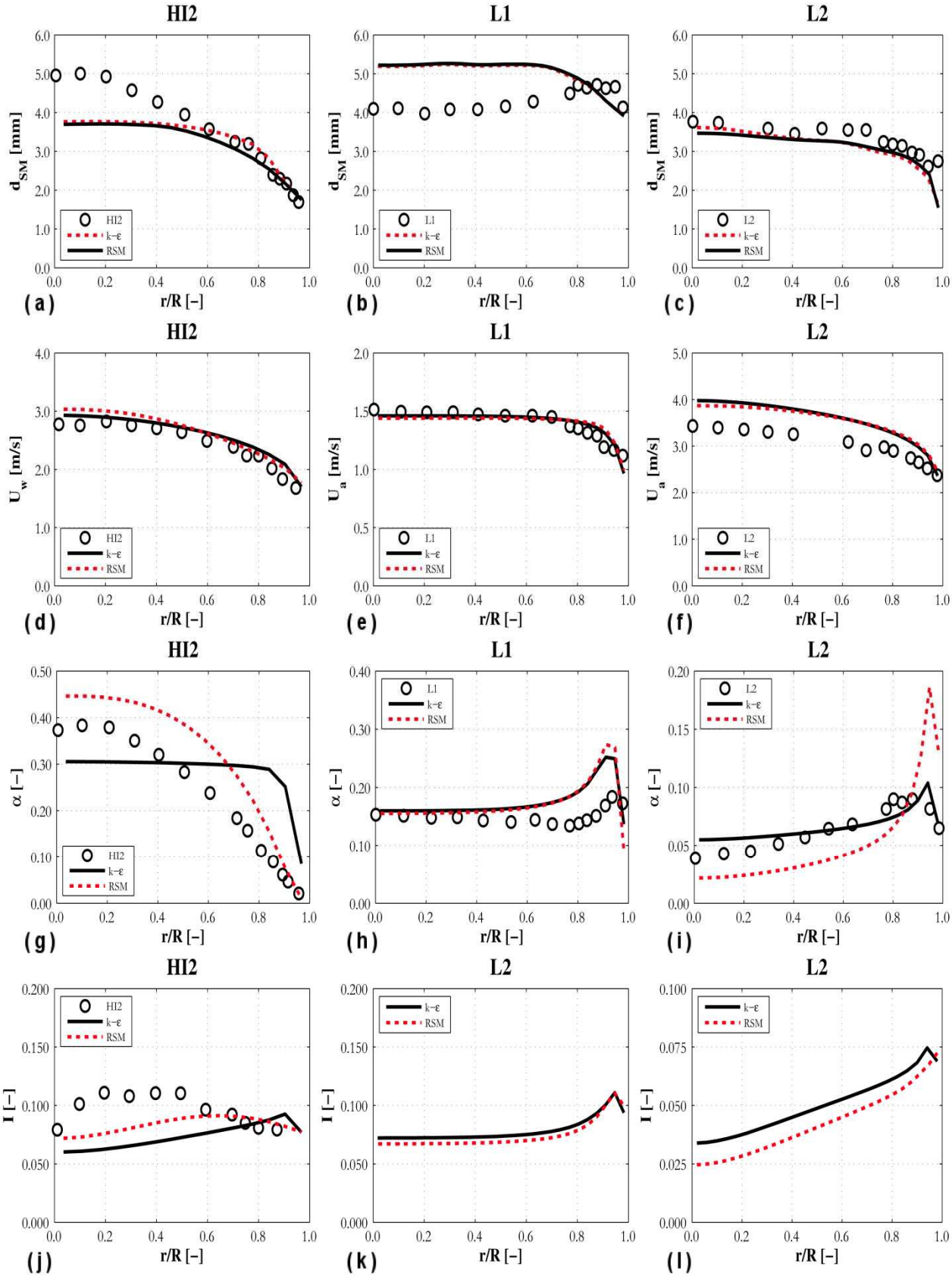

Figure 11. SMD (a-c), mean velocity (d-f), void fraction (g-i) and turbulence intensity (j-l) radial profiles compared against experiments HI2, L1 and L2. Predictions were obtained with a *k-ε* (—) and a Reynolds stress (---) turbulence formulation.

4.4. Two-group model

It was mentioned in the introduction how bubbly flows are generally characterized by polidispersity and by an extended range of bubble sizes. The comparisons in the previous sections demonstrated the different behaviour of spherical and larger cap bubbles, showing wall-peaked or core-peaked void fraction profiles induced by the value of the average bubble diameter. When both types of bubble are present in a comparable amount, the void fraction profile may exhibit both wall- and core-peaked features, as is the case for the experiment L1, depicted in Figure 12 (Lucas et al., 2005). These experiments are particularly difficult to predict because the distinctive features of both bubble types must be reproduced. Therefore, an advanced model with two different bubble classes was specifically implemented to predict these kinds of flows. In view of the results from the previous sections, and the in general negligible impact of break-up, only the additional sources due to the coalescence of two spherical bubbles into a cap bubble were considered. For this case, the value of the critical diameter d_c was assumed equal to 5 mm. Comparison against experimental data is provided in Figure 12, based on the RSM predictions. As shown in the figure, the void fraction radial profile and the behaviour of both the spherical and the cap bubbles are well predicted. Near the wall, the void fraction profile increases rapidly because of the presence there of the majority of the spherical bubbles. After a region where it remains almost flat, the void fraction increases again towards the pipe centre where the cap bubbles accumulate, pushed there by the negative lift force. In a similar manner, close to the wall, the average bubble diameter is close to the average diameter of the spherical bubbles, whereas it tends to the average diameter of the cap bubbles towards the pipe centre.

The bubble size distribution, which is tracked by the S_y model, is shown at three different axial locations in Figure 13. The plots display h_{dB}, which is, following the work of Lucas et al. (2005), the contribution of each bubble size to the total void fraction:

$$h_{d_B} = \frac{d(\alpha)}{d(d_B)} \tag{44}$$

796

797 In this way, the contribution of larger bubbles, which are few in number but carry a significant
798 amount of the total air volume, is properly accounted for (Lucas et al., 2005). Experimental data
799 were obtained by averaging over the whole pipe cross-section. For the predictions, the bubble
800 distribution was extracted from the simulation at each node and is shown in Figure 13 for the near-
801 wall region (Figure 13a) and for the pipe centre (Figure 13b). At the first axial location (*L/D* = 8.4),
802 two distinct peaks are shown in both the experimental and the numerical results. Starting from the
803 inlet, the predominance of coalescence events leads to the formation of larger bubbles, as is
804 demonstrated by the second peak in the profile at around 6 mm. Obviously, being still close to the
805 inlet, large bubbles represent only a small fraction of the total void fraction. At this location, the
806 total void fraction is overestimated, as can be seen from the higher peak values predicted. This is
807 due to the fact that it was not possible to match the inlet conditions of the experiment exactly due to
808 lack of data, in particular for the velocity of the phases. Therefore, some distance from the inlet is
809 required for the flow to establish. Predicted values of the void fraction at the two other locations are
810 indeed significantly closer to the experimental values. At the second axial location (*L/D* = 29.9), the
811 bubble population evolves and, since coalescence remains predominant, the number of larger
812 bubbles increases. Two distinctive peaks are still present, but the larger diameter peak is now the
813 greatest. This shift of the bubble diameter spectrum to larger values is well reproduced by the
814 simulation, with the main difference with experiment being a larger number of bubbles in the region
815 between the two peaks. At the final location (*L/D* = 59.2), the larger bubbles are in the majority,
816 with the first peak at around 4 mm now being very small. The same evolution is found in the
817 simulation, with a more diffuse distribution and an extended spectrum of diameters. It should be
818 noted that the variance of the distribution is lower and the first peak still present near the wall where
819 the majority of the spherical bubbles are present. In contrast, near the pipe centre, where the

majority of the larger bubbles accumulate, the averaged experimental spectrum is overestimated and the bubble population extends to even higher values of the bubble diameter. The experimental profile, therefore, can be qualitatively considered an average of these two behaviours. In view of these results, the evolution of the bubble diameter distribution is predicted with a satisfactory accuracy, even with the rather simple model adopted which could be subject to numerous further improvements. Therefore, the challenge of predicting the whole bubble size spectrum from small spherical to large cap bubbles seems to be manageable with the use of only two bubble groups.

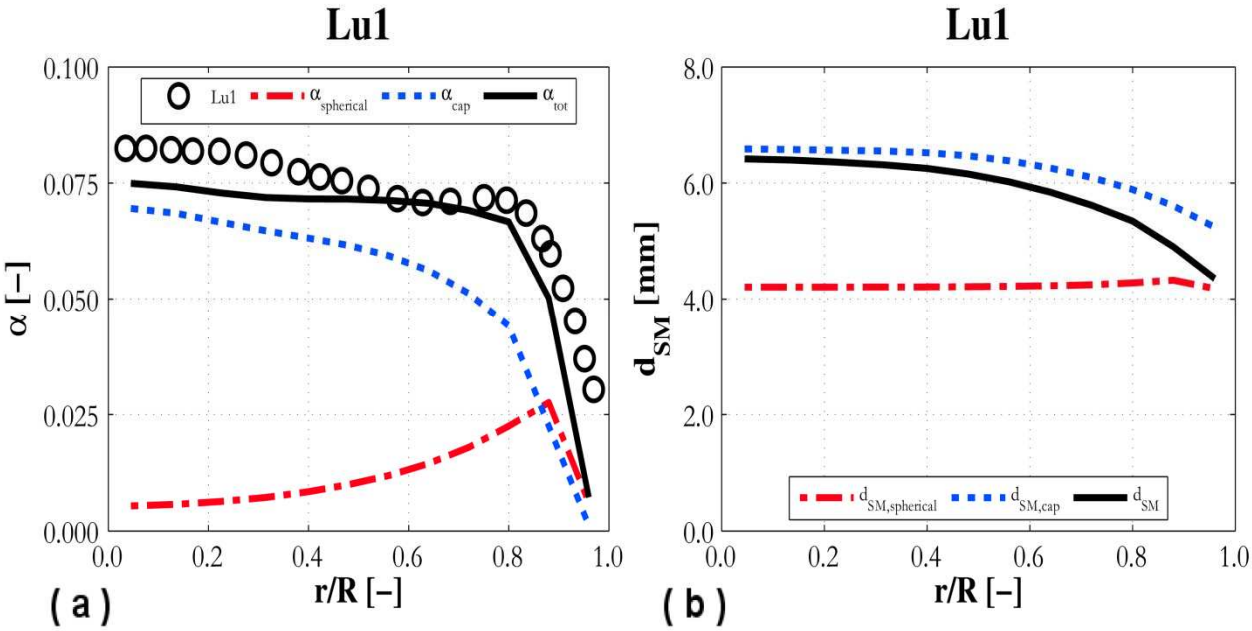

Figure 12. Void fraction (a) and SMD (b) radial profiles considering two bubble classes. Along with total values (—), which are compared against Lu1 experiment, predictions for spherical (-·-) and cap bubbles (---) are also shown.

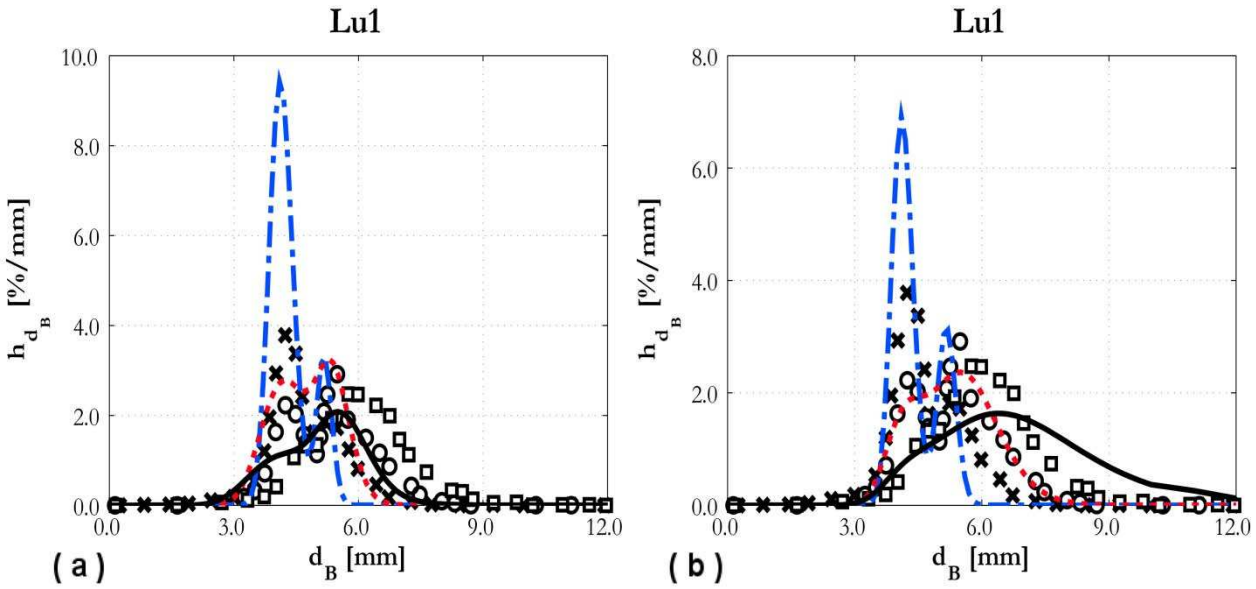

Figure 13. Bubble diameter distribution extracted from the simulations (lines) compared against the experiments (markers) at three axial locations: L/D = 8.4 (x, -·-); L/D = 29.9 (○, --); L/D = 59.2 (□, —). Simulation results are displayed in two different locations: (a) pipe wall; (b) pipe centre.

5. Conclusions

In this work, the S_γ model (Lo and Zhang, 2009), based on the moments of the bubble size distribution, was coupled with an Eulerian-Eulerian two-fluid model with the STAR-CCM+ code, and tested against the data from seven upward bubbly flow experiments in pipes. Through the S_γ model, the evolution of the bubble size distribution was followed through the flows, so that the average SMD and the interfacial area concentration, which are crucial for the prediction of the phase interactions, could be tracked. Being based on the method of moments, the S_γ model also has the advantage that the required computational resources are limited. The addition of a different coalescence model (Yao and Morel, 2004), based on the collision of bubbles in turbulence and on the film drainage model, and further optimized against the experiments, allowed reproduction of the experimental radial profiles of the average bubble diameter. More specifically, a constant critical Weber number value of 0.10 in the coalescence model was sufficient to obtain a satisfactory predictive accuracy.

A sensitivity study suggested a negligible effect of the bubble break-up model and the best results were achieved by considering these flows to be dominated by bubble coalescence. However, the lack of availability of experimental data, limited to the average bubble diameter alone, constrains research work in the field. In particular, it is extremely difficult to evaluate the competitive contributions of break-up and coalescence, and to extend the modelling to cover all possible mechanisms involved. Therefore, additional knowledge is required, by means of experiments or direct numerical simulations. Continuous phase turbulence was noted to significantly influence the predictions of the model. In this regard, validation of turbulence models needs to be carried out in conjunction with that for the bubble diameter evolution, and requires the availability of additional complete datasets. In addition, different coalescence models were found to display different qualitative behaviour following changes in the flow field turbulence level, and this requires further investigation.

Lastly, an advanced version of the overall model described was tested. This included a Reynolds stress turbulence formulation and two groups of bubbles, accounting for spherical bubbles accumulating close to the wall and cap bubbles migrating towards the pipe centre. The RSM, in addition to performing better in flows where known shortcomings of two-equation turbulence models are present, provides better accuracy in predicting core-peaked void fraction profiles and properly accounts for the interaction between the turbulence and the interphase forces. Comparison with a complex void fraction profile suggested that extension of the model to only two bubble groups is sufficient to describe the whole bubble spectrum, and the bubbly flow regime up to the transition to slug flow, even though additional comparisons with data are necessary.

Acknowledgements

The authors gratefully acknowledge the financial support of the EPSRC under grant EP/K007777/1, Thermal Hydraulics for Boiling and Passive Systems, part of the UK-India Civil Nuclear

881 Collaboration. The authors are also grateful to Dr. Andrew Splawski and Dr. Simon Lo from CD-
882 adapco for the valuable technical and scientific support.

883

884 ## References

885 Antal, S.P., Lahey Jr, R.T., Flaherty, J.E., 1991. Analysis of phase distribution in fully developed
886 laminar bubbly two-phase flow. Int. J. Multiphas. Flow 17, 635-652.

887 Auton, T.R., 1987. The lift force on a spherical body in a rotational flow. J. Fluid Mech. 183, 199-
888 218.

889 Behzadi, A., Issa, R.I., Rusche, H., 2004. Modelling of dispersed bubble and droplet flow at high
890 phase fractions. Chem. Eng. Sci. 59, 759-770.

891 Buffo, A., Vanni, M., Marchisio, D.L., Fox, R.O., 2013. Multivariate Quadrature-Based Moments
892 Methods for turbulent polydisperse gas-liquid systems. Int. J. Multiphas. Flow 50, 41-57.

893 Burns, A.D., Frank, T., Hamill, I., Shi, J.M., 2004. The Favre averaged drag model for turbulent
894 dispersion in Eulerian multi-phase flows. 5th International Conference on Multiphase Flow,
895 Yokohama, Japan, May 30 – June 4, paper 392.

896 CD-adapco, 2014. STAR-CCM+® Version 9.06 User Guide.

897 Chester, A.K., 1988. Local coalescence rates in emulsions: a model for collision and film thinning
898 process when drop inertia dominates. BRITE Report I-31.

899 Chester, A.K., 1991. The modeling of coalescence processes in fluid-liquid dispersions: A review of
900 current understanding. Chem. Eng. Res. Des.: T I Chem. Eng.-Lond. 69(A), 259-270.

901 Cheung, S.C.P., Deju, L., Yeoh, G.H., Tu, J.Y., 2013. Modelling of bubble-size distribution in
902 isothermal gas-liquid flows: numerical assessment of population balance approaches. Nucl. Eng.
903 Des. 265, 120-136.

904 Cheung, S.C.P., Yeoh, G.H., Tu, J.Y., 2009. A review of population balance modelling for
905 isothermal bubbly flows. J. Comput. Multiphas. Flow 1, 161-199.

906 Cheung, S.C.P., Yeoh, G.H., Tu, J.Y., 2007. On the modelling of population balance in isothermal
907 vertical bubbly flos-Average bubble number density approach. Chem. Eng. Process. 46, 742-756.

908 Colombo, M., Fairweather, M., Lo, S., Splawski, A., 2015. Multiphase RANS simulation of
909 turbulent bubbly flows. 16th International Topical Meeting on Nuclear Reactor Thermal
910 Hydraulics, Chicago, USA, August 30 – September 4.
911 Dabiri, S., Tryggvason, G., 2015. Heat transfer in turbulent bubbly flow in vertical channels. Chem.
912 Eng. Sci. 122, 106-113.
913 Daly, B.J., Harlow, F.H., 1970. Transport equations of turbulence. Phys. Fluids 13, 2634-2649.
914 Fox, R., 2012. Large-Eddy-Simulation tools for multiphase flows. Annu. Rev. Fluid Mech. 44, 47-
915 76.
916 Gosman, A.D., Lekakou, C., Politis, S., Issa, R.I., Looney, M.K., 1992. Multidimensional modeling
917 of turbulent two-phase flows in stirred vessels. AIChE J. 38, 1946-1956.
918 Grossetete, C., 1995. Experimental investigation and preliminary numerical simulations of void
919 profile development in a vertical cylindrical pipe. In: Serizawa, A., Fukano, T., Bataille, J.
920 (Eds.), 2nd International Conference on Multiphase Flow, Kyoto, Japan, April 3-7, IF1-1-10.
921 Hibiki, T., Ishii, M., 1999. Experimental study on interfacial area transport in bubbly two-phase
922 flows. Int. J. Heat Mass Tran. 42, 3019-3035.
923 Hibiki, T., Ishii, M., 2000. One-group interfacial area transport of bubbly flows in vertical round
924 tubes. Int. J. Heat Mass Tran. 43, 2711-2726.
925 Hibiki, T., Ishii, M., Xiao, Z., 2001. Axial interfacial area transport of vertical bubbly flows. Int. J.
926 Heat Mass Tran. 44, 1869-1888.
927 Hosokawa, S., Tomiyama, A., 2009. Multi-fluid simulation of turbulent bubbly pipe flow. Chem.
928 Eng. Sci. 64, 5308-5318.
929 Hulburt, H.M., Katz, S., 1964. Some problems in particle technology. Chem. Eng. Sci. 19, 555-574.
930 Ishii, M., Hibiki, T., 2006. Thermo-fluid dynamics of two-phase flows. Springer.
931 Jones, W.P., Launder, B.E., 1972. The prediction of laminarization with a two-equation model of
932 turbulence. Int. J. Heat Mass Tran. 15, 301-314.

933 Kataoka, I., Serizawa, A., 1989. Basic equations of turbulence in gas-liquid two-phase flow. Int. J.
934 Multiphas. Flow 15, 843-855.
935 Krepper, E., Lucas, D., Frank, T., Prasser, H.M., Zwart, P.J., 2008. The inhomogeneous MUSIG
936 model for the simulation of polydispersed flows. Nucl. Eng. Des. 238, 1690-1702.
937 Kumar, S., Ramkrishna, D., 1996. On the solution of population balance equations by discretization
938 –I. A fixed pivot technique. Chem. Eng. Sci. 51(8), 1311-1332.
939 Lahey Jr, R.T., Drew, D.A., 2001. The analysis of two-phase flow and heat transfer using a
940 multidimensional, four field, two-fluid model. Nucl. Eng. Des. 204, 29-44.
941 Lance, M., Bataille, J., 1991. Turbulence in the liquid phase of a uniform bubbly air-water flow. J.
942 Fluid Mech. 222, 95-118.
943 Lee, K., Matsoukas, T., 2000. Simultaneous coagulation and break-up using constant-*N* Monte
944 Carlo. Powder Technol. 110, 82-89.
945 Lehr, F., Millies, M., Mewes, D., 2002. Bubble-size distributions and flow fields in bubble
946 columns. AIChE J. 48(11), 2426-2441.
947 Liao, Y., Lucas, D., 2009. A literature review of theoretical models for drop and bubble breakup in
948 turbulent dispersions. Chem. Eng. Sci. 64, 3389-3406.
949 Liao, Y., Lucas, D., 2010. A literature review on mechanisms and models for the coalescence
950 process of fluid particles. Chem. Eng. Sci. 65, 2851-2864.
951 Liao, Y., Rzehak, R., Lucas, D., Krepper, E., 2015. Baseline closure model for dispersed bubbly
952 flow: bubble coalescence and breakup. Chem. Eng. Sci. 122, 336-349.
953 Lin, Y., Lee, K., Matsoukas, T., 2002. Solution of the population balance equation using constant-
954 number Monte Carlo. Chem. Eng. Sci. 57, 2241-2252.
955 Liu, T.J., 1993. Bubble size and entrance length effects on void development in a vertical channel.
956 Int. J. Multiphas. Flow 19(1), 99-113.
957 Liu, T.J., Bankoff, S.G., 1993. Structure of air-water bubbly flow in a vertical pipe – I. Liquid mean
958 velocity and turbulence measurements. Int. J. Heat Mass Tran. 36, 1049-1060.

959 Liu, T.J., 1998. The role of bubble size on liquid phase on liquid phase turbulent structure in two-
960 phase bubbly flows. Proceedings of the 3rd International Conference on Multiphase Flow, Lyon,
961 France, June 8-12.
962 Lo, S., 1996. Application of the MUSIG model to bubbly flows. AEAT-1096, AEA Technology.
963 Lo, S., Rao, P., 2007. Modelling of droplet breakup and coalescence in an oil-water pipeline. 6th
964 International Conference on Multiphase Flow, Leipzig, Germany, July 9-13, Paper 136.
965 Lo, S., Zhang, D., 2009. Modelling of break-up and coalescence in bubbly two-phase flows. J.
966 Comput. Multiphas. Flow 1, 23-38.
967 Lopez de Bertodano, M., Lahey Jr, R.T., Jones, O.C., 1994. Phase distribution in bubbly two-phase
968 flow in vertical ducts. Int. J. Multiphas. Flow 20, 805-818.
969 Lucas, D., Beyer, M., Szalinski, L., Schutz, P., 2010. A new database on the evolution of air-water
970 flows along a large vertical pipe. Int. J. Therm. Sci. 49, 664-674.
971 Lucas, D., Krepper, E., Prasser, H.M., 2005. Development of co-current air-water flow in a vertical
972 pipe. Int. J. Multiphas. Flow 31, 1304-1328.
973 Luo, H., Svendsen, H.F., 1996. Theoretical model for drop and bubble breakup in turbulent
974 dispersions. AIChE J. 42(5), 1225-1233.
975 Marchisio, D.L., Fox, R.O., 2005. Solution of population balance equations using the direct
976 quadrature method of moments. Aerosol Sci. 36, 43-73.
977 Marchisio, D.L., Fox, R.O., 2007. Multiphase reacting flows: modelling and simulation. Springer.
978 Molin, D., Marchioli, C., Soldati, A., 2012. Turbulence modulation and microbubble dynamics in
979 vertical channel flow. Int. J. Multiphas. Flow 42, 80-95.
980 Mukin R.V., 2014. Modeling of bubble coalescence and break-up in turbulent bubbly flow. Int. J.
981 Multiphas. Flow 62, 52-66.
982 Nandanwar, M.N., Kumar, S., 2008. A new discretization of space for the solution of multi-
983 dimensional population balance equations. Chem. Eng. Sci. 63, 2198-2210.

984 Nguyen, V.T., Song, C.H., Bae, B.U., Euh, D.J., 2013. Modeling of bubble coalescence and break-
985 up considering turbulent suppression phenomena in bubbly two-phase flow. Int. J. Multiphas.
986 Flow 54, 31-42.
987 Prasser, H.M., Beyer, M., Carl, H., Gregor, S., Lucas, D., Pietruske, H., Schutze, P., Weiss, F.P.,
988 2007. Evolution of the structure of a gas-liquid two-phase flow in a large vertical pipe. Nucl.
989 Eng. Des. 237, 1848-1861.
990 Prince, M.J., Blanch, H.W., 1990. Bubble coalescence and break-up in air-sparged bubble columns.
991 AIChE J. 36(10), 1485-1499.
992 Prosperetti, A., Tryggvason, G., 2009. Computational methods for multiphase flow. Cambridge
993 University Press.
994 Rzehak, R., Krepper, E., 2013. CFD modeling of bubble-induced turbulence. Int. J. Multiphas.
995 Flow 55, 138-155.
996 Santarelli, C., Roussel, J., Fröhlich, J., 2016. Budget analysis of the turbulent kinetic energy for
997 bubbly flow in a vertical channel. Chem. Eng. Sci. 141, 46-62.
998 Sanyal, J., Vasquez, S., Roy, S., Dudukovic, M.P., 1999. Numerical simulation of gas-liquid
999 dynamics in cylindrical bubble column reactors. Chem. Eng. Sci. 54, 5071-5083.
1000 Serizawa, A., Kataoka, I., Michiyoshi, I., 1975. Turbulence structure of air-water bubbly flow-II.
1001 Local properties. Int. J. Multiphas. Flow 2, 235-246.
1002 Shawkat, M.E., Ching, C.Y., Shoukri, M., 2007. On the liquid turbulence energy spectra in two-
1003 phase bubbly flow in a large diameter pipe. Int. J. Multiphas. Flow 33, 300-316.
1004 Smith, T.R., Schlegel, J.P., Hibiki, T., Ishii, M., 2012. Mechanistic modeling of interfacial area
1005 transport in large diameter pipes. Int. J. Multiphas. Flow 47, 1-16.
1006 Speziale, C.G., Sarkar, S., Gatski, T.B., 1991. Modelling the pressure-strain correlation of
1007 turbulence: An invariant dynamical system approach. J. Fluid Mech. 227, 245-272.
1008 Sun, X., Kim, S., Ishii, M., Beus, S.G., 2004. Modeling of bubble coalescence and disintegration in
1009 confined upward two-phase flow. Nucl. Eng. Des. 230, 3-26.

1010 Tomiyama, A., Tamai, H., Zun, I., Hosokawa, S., 1998. Transverse migration of single bubbles in
1011 simple shear flows. Chem. Eng. Sci. 57, 1849-1858.
1012 Tomiyama, A., Celata, G.P., Hosokawa, S., Yoshida, S., 2002a. Terminal velocity of single bubbles
1013 in surface tension dominant regime. Int. J. Multiphas. Flow 28, 1497-1519.
1014 Tomiyama, A., Tamai, H., Zun, I., Hosokawa, S., 2002b. Transverse migration of single bubbles in
1015 simple shear flows. Chem. Eng. Sci. 57, 1849-1858.
1016 Toutant, A., Labourasse, E., Lebaigue, O., Simonin, O., 2008. DNS of the interaction between a
1017 deformable buoyant bubble and a spatially decaying turbulence: A priori test for LES two-phase
1018 flow modelling. Comput. Fluids 37, 877-886.
1019 Troshko, A.A., Hassan, Y.A., 2001. A two-equation turbulence model of turbulent bubbly flows.
1020 Int. J. Multiphas. Flow 27, 1965-2000.
1021 Tryggvason, G., Buongiorno, J., 2010. The role of direct numerical simulations in validation and
1022 verification. Computational Fluid Dynamics (CFD) for Nuclear Reactor Safety Applications
1023 OECD-NEA Workshop, Bethesda, USA September 14-16.
1024 Ullrich, M., Maduta, R., Jakirlic, S., 2014. Turbulent bubbly flow in a vertical pipe computed by an
1025 eddy-resolving Reynolds stress model. 10th International ERCOFTAC Symposium on
1026 Engineering Turbulence Modelling and Measurements, Marbella, Spain, September 17-19.
1027 Vanni, M., 2000. Approximate population balance equations for aggregation-breakage processess.
1028 J. Colloid Interf. Sci. 221, 143-160.
1029 Wang, S.K., Lee, S.J., Jones Jr, O.C., Lahey Jr, R.T., 1987. 3-D turbulence structure and phase
1030 distribution measurements in bubbly two-phase flows. Int. J. Multiphas. Flow 13, 327-343.
1031 Wang, T., Wang, J., Jin, Y., 2005. Theoretical prediction of flow regime transition in bubble
1032 columns by the population balance model. Chem. Eng. Sci. 60, 6199-6209.
1033 Welleck, R.M., Agrawal, A.K., Skelland, A.H.P., 1966. Shape of liquid drops moving in liquid
1034 media. AIChE J. 12, 854-862.

1035 Wu, K., Kim, S., Ishii, M., Beus, S.G., 1998. One-group interfacial area transport in vertical bubbly
1036 flow. Int. J. Heat Mass Tran. 41, 1103-1112.
1037 Yao, W. and Morel, C., 2004. Volumetric interfacial area prediction in upward bubbly two-phase
1038 flow. Int. J. Heat Mass Tran. 47, 307-328.
1039 Yuan, C., Fox, R.O., 2011. Conditional quadrature method of moments for kinetic equations. J.
1040 Comput. Phys. 230, 8216-8246.
1041 Zhao, H., Maisels, A., Matsoukas, T., Zheng, C., 2007. Analysis of four Monte-Carlo methods for
1042 the solution of population balances in dispersed systems. Powder Technol. 173, 38-50.

1043
1044